Advanced Lab Course

Fortgeschrittenpraktikum (FOPRA)

High-Resolution X-ray Diffraction

October 2020

Chair of Experimental Semiconductor Physics

Walter Schottky Institute

Technical University of Munich

Am Coulombwall 4

85747 Garching

Table of Content

1. Crystals 3

1.1. Ideal Crystals 3

1.1.1. Definition 3

1.1.2. Miller Indices 4

1.2. Real Crystals 6

2. Theory of X-ray Diffraction 11

2.1. Kinetic Theory of X-ray Diffraction 11

2.2. Reciprocal Lattice 12

2.3. X-ray Diffraction at Periodic Structures 14

2.4. Bragg Equation 15

2.5. Ewald Sphere 15

2.6. Structure Factor 17

3. Experimental Setup 19

4. Characterization of Real Crystals by HRXRD 21

4.1. 2Theta-Omega Scan 21

4.2. Omega Scan 23

4.3. Reciprocal Space Map 27

4.4. Phi Scan 28

5. Pre-Measurement Exercises 29

6. Experimental Procedure 30

6.1. Optics Alignment 30

6.2. Sample A Alignment 31

6.3. Sample A 33

6.4. Sample B 37

6.5. Sample C 41

6.6. Post-Measurement 41

7. Report 42

8. References 43

Appendix A Measurement Report Sheet 44

Appendix B Theoretical 2θ and τ values of ZnO and Al_2O_3 47

1. Crystals

At the end of the 19th century the micro structure of solids was still under debate. *Max von Laue* had the idea to clarify this issue by using X-rays which were discovered some 20 years before by *Wilhelm Conrad Röntgen*. For this purpose, *von Laue* worked out a theory for X-ray diffraction at three-dimensional crystals. With the observation of diffraction patterns by irradiating solids with X-rays, his coworkers *Walther Friedrich* and *Paul Knipping* verified both the periodic space structure of most solids and the wave character of X-rays.

In this laboratory exercise we will address the structural characterization of solids by means of high-resolution X-ray diffraction (HRXRD). In general, this technique is not used to determine the crystal structure, but to investigate deviations from an ideal crystal which can be induced i.e. by defects, mosaicity or strain.

We first give an overview on the basic concepts of how to describe an ideal crystal. Subsequently, we treat irregularities and defects in real crystals. We then give an introduction in the kinematic theory of X-ray diffraction. Finally, the experimental setup is presented and the characterization of real crystals by HRXRD is discussed.

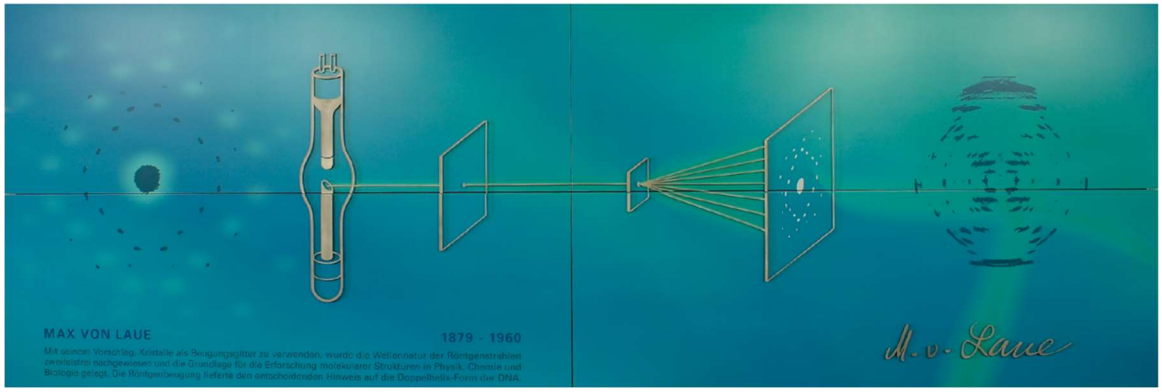

Figure 1: Irradiation of a thin slab of a crystal with “white” X-rays produced a distinct diffraction pattern. Picture taken at the U-Bahn station Garching-Forschungszentrum.

1.1. Ideal Crystals

1.1.1. Definition

An ideal crystal is an infinite, periodic array of a structural element. The structural element which consists of an atom or a group of (identical or different) atoms is called *basis*. A crystal can be built up by repeatedly placing the basis at well-defined lattice sites which constitute the so-called space lattice. The arrangement of the atoms looks identical viewed from every point of the space lattice. The lattice points can be reached by a translation

$$\boldsymbol{r} = n_1\boldsymbol{a_1} + n_2\boldsymbol{a_2} + n_3\boldsymbol{a_3} \qquad (1)$$

where all n_i are integer. The lattice vectors a_i have to be linearly independent. They span the unit cell, whose volume V_{uc} is given by the scalar triple product

$$V_{uc} = \boldsymbol{a_1} \cdot (\boldsymbol{a_2} \times \boldsymbol{a_3}) \tag{2}$$

The unit cell with the smallest volume possible is called primitive unit cell, and it is spanned by the primitive lattice vectors. The number of atoms that its associated basis contains is as small as possible. For a given basis there is an infinite number of possible choices for the unit cell (Figure 2). Yet the volume of all possible unit cells is always the same. In order to take into account other symmetries of the crystal than the translational symmetry, like rotational or mirror symmetry, it is often reasonable to choose a non-primitive unit cell, or so-called conventional unit cell. However, this results in a more complex structure of the basis of the crystal.

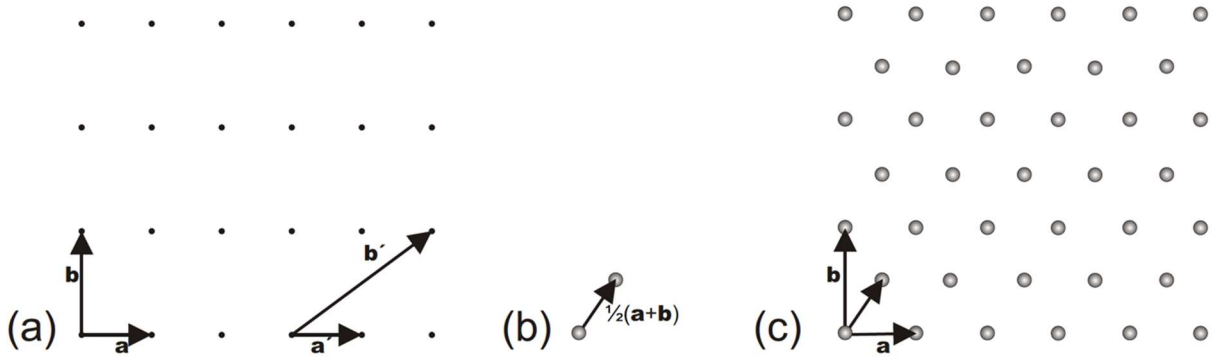

Figure 2: (a) Space lattice with two different choices of unit cells (b) basis (c) resulting two-dimensional crystal.

1.1.2. Miller Indices

Any plane containing lattice points is called a lattice plane. In an ideal crystal there is always an infinite number of parallel lattice planes. As we will see later, it is convenient to label a set of parallel lattice planes according to the following algorithm:

1. Determine the intersection points *a*, *b* and *c* of any of the lattice planes with the coordinate axes in units of the lattice constants, i.e. in multiples of the lengths of the lattice vector $\mathbf{a_i}$.

2. Take the reciprocal values $h' = \frac{1}{a}$, $k' = \frac{1}{b}$, and $l' = \frac{1}{c}$.

3. Multiply these values with the smallest number m possible so that $h = m \cdot h'$, $k = m \cdot k'$, $l = m \cdot l'$ are integer.

The thus obtained triple (hkl) is known as Miller indices. For example, if one lattice plane intersects the axes at *a = –2*, *b = 1* and *c = 4*, the set of parallel planes it belongs to is

labeled by the Miller indices $(\bar{2}41)$. Negative values are marked with a bar over the index. If the lattice plane is parallel to an axis, the intersection point is ∞ and therefore the corresponding index is equal to 0. To indicate that the triple (hkl) labels all parallel lattice planes, it is enclosed in parentheses. To designate crystallographically equivalent planes, the Miller indices are enclosed in curly braces $\{hkl\}$. For instance, lattice planes limiting the unit cell in a cubic lattice, i.e. the (100), (010), (001), $(\bar{1}00)$, $(0\bar{1}0)$ and $(00\bar{1})$ planes, can be subsumed by writing $\{100\}$. Similarly, directions in the lattice are indicated by a triple of integers $[uvw]$ enclosed in square brackets. *u*, *v* and *w* denote the smallest possible integer components of a vector $\boldsymbol{R} = u\boldsymbol{a} + v\boldsymbol{b} + w\boldsymbol{c}$ pointing along the designated direction.

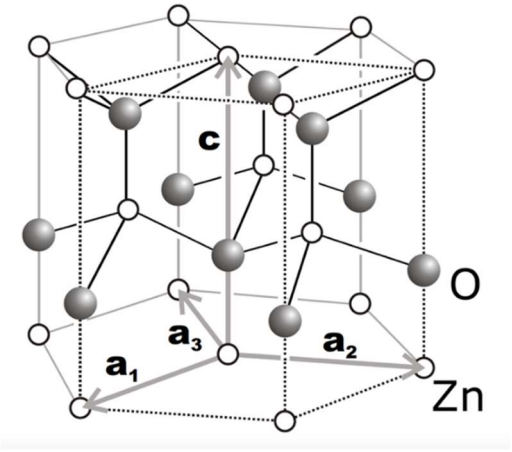

Figure 3: Hexagonal unit cell of the Wurtzite lattice. Its primitive unit cell is limited by the lattice vector $\mathbf{a}_1$, $\mathbf{a}_2$, and **c** as well as the dotted lines and it contains four atoms.

In this laboratory exercise we will investigate thin zinc oxide (ZnO) and zinc magnesium oxide (ZnMgO) films which have crystallized in a hexagonal Wurtzite lattice. The Zn and O atoms form two interpenetrating, hexagonal close-packed sublattices which are displaced along the *c*-direction of their hexagonal unit cell (Figure 3). In this structure the Zn (O) atoms are tetrahedrally coordinated which means that they are situated at the center of a tetrahedron which is formed by O (Zn) atoms. The atoms are usually grouped in bilayers, which consist of two adjacent (00.1) lattice planes (the signification of the dot in this notation is explained below). The staking order of the bilayers is ABABAB. . . (Figure 4).

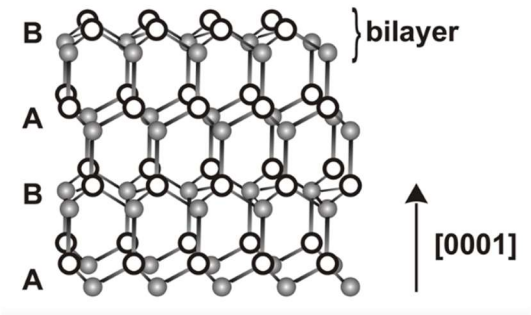

Figure 4: Side-view of a Wurtzite crystal showing that its bilayers are stacked in the sequence ABABAB.

In Figure 3 the hexagonal unit cell of the Wurtzite lattice is shown. It is spanned by the lattice vectors $\mathbf{a_1}$ and $\mathbf{a_2}$ lying in the basal plane as well as **c** being perpendicular hereon. The basis of the Wurtzite lattice consists of four atoms. By using the above described methods to label directions and planes, in hexagonal crystals crystallographically equivalent directions and planes can be designated by a different type of triple (hkl) or$[hkl]$. For example, the crystallographically equivalent planes limiting the unit cell parallel to the *c*-direction can be labeled $(1\bar{1}.0)$ and (10.0) (Figure 5(a)). Therefore, it is common to use a coordinate system with four axes and a quadruple of integers for indexing. This takes into account that there are three equivalent symmetry axes $\mathbf{a_1}$, $\mathbf{a_2}$ and $\mathbf{a_3}$ in the plane perpendicular to the principal axis along the *c*-direction. The indices $(hkil)$ are then determined analogously to the already presented algorithm. Thereby the relation

$$i = -(h + k) \tag{3}$$

is valid, because $\mathbf{a_1}$, $\mathbf{a_2}$ and $\mathbf{a_3}$ are not linearly independent as $\mathbf{a_3} = -(\mathbf{a_1} + \mathbf{a_2})$. For designating directions, one has to assure to pick that linear combination of lattice vectors that satisfies equation (3). For instance, the direction along the $-\mathbf{a_2}$ vector is not labeled $[0\bar{1}00]$ but $[1\bar{2}10]$ (Figure 5(b)). If one chooses to use only three indices in a hexagonal lattice, one places usually a dot, that shall represent the omitted fourth index, between the second and third index $[hk.l]$. Then, equation (3) does not to be obeyed. Using four indices for indexing has the advantage that crystallographically equivalent directions and planes are obtained by a simple cyclic permutation of the indices.

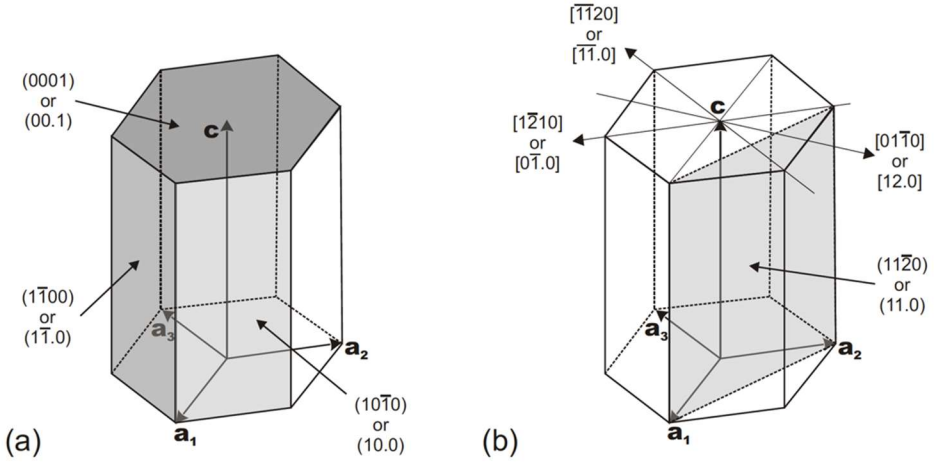

Figure 5: Indexing of directions and planes in a hexagonal lattice.

1.2. Real Crystals

In real crystals the requirement to minimize the free energy $F = U - TS$ induces deviations from the ideal crystal structure. Already small concentrations of defects can

drastically influence the properties of crystals. For example, the electrical conductivity of a semiconductor can be significantly increased by the incorporation of a small amount of extrinsic impurities, which is typically known as doping. It is therefore important to investigate the nature and density of defects. For this purpose, HRXRD is a suitable method that does not damage the samples, and no complex sample preparation is required. In this laboratory exercise, we investigate heteroepitaxially grown thin films. This means that the underlying substrate and the epitaxial layer are different materials with typically different lattice constants, and perhaps even of different crystal symmetry. To quantify the difference in lattice constant the so-called lattice mismatch $\Delta a/a$ is defined as follows

$$\frac{\Delta a}{a} = \frac{a_{substrate} - a_{film}^{relax}}{a_{substrate}} \tag{4}$$

where $a_{substrate}$ and a_{film}^{relax} refer to the respective relaxed lattice constants (see Figure 6) in the plane parallel to the interface. For a small lattice mismatch, the epitaxial film can grow pseudomorphical, i.e. it adapts the in-plane lattice constant of the substrate thereby accumulating biaxial strain (Figure 6(b)).

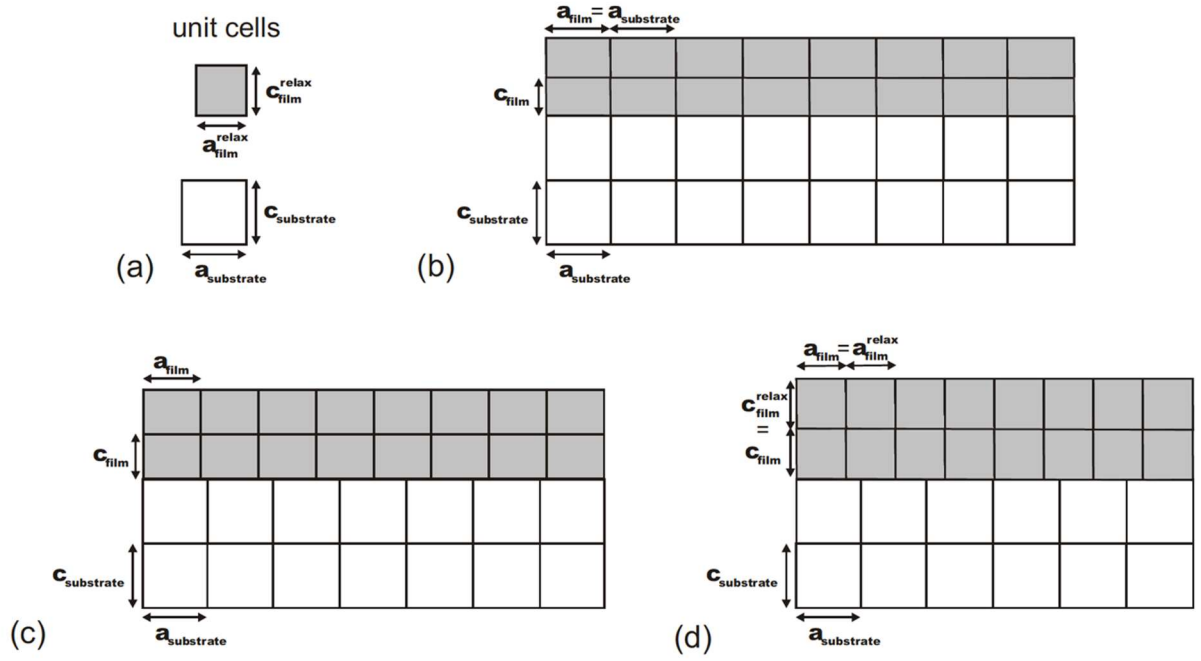

Figure 6: (a) Relaxes unit cells of film and substrate. Schematic representation of (b) a pseudomorphical, (c) a partially relaxed, and (d) a fully relaxed heteroepitaxial film.

When the film thickness exceeds a certain critical value, the built-up strain energy is released by the formation of one-dimensional defects, called dislocations, perpendicular to the interface. In the vicinity of a dislocation the crystal lattice is distorted and strain is accumulated, that decays rather slowly as one moves away from the dislocation. By moving along a 360°-loop around a dislocation, one does not arrive at one's starting point. The difference between starting and end points defines the *Burgers vector* **b**. In general, two types

of dislocations can be distinguished, namely *screw*- and *edge-type dislocations* (Figure 7). For screw-type dislocations the Burgers vector **b** is oriented along the dislocation, whereas for edge-type dislocation it is perpendicular. Dislocations have the tendency to arrange themselves in the most stable configuration possible. Therefore, for example edge-type dislocations prefer to group themselves together, as shown in Figure 8, in order to minimize the strain energy. Such an agglomeration of dislocations is known as *grain boundary*. This type of two-dimensional defect can be seen as a boundary between two monocrystalline regions of a solid, called *crystallites*, which are twisted by an angle δ with respect to one another. In a similar way as edge-type dislocations result in a twist, screw-type dislocations can give rise to a tilt of the crystallites.

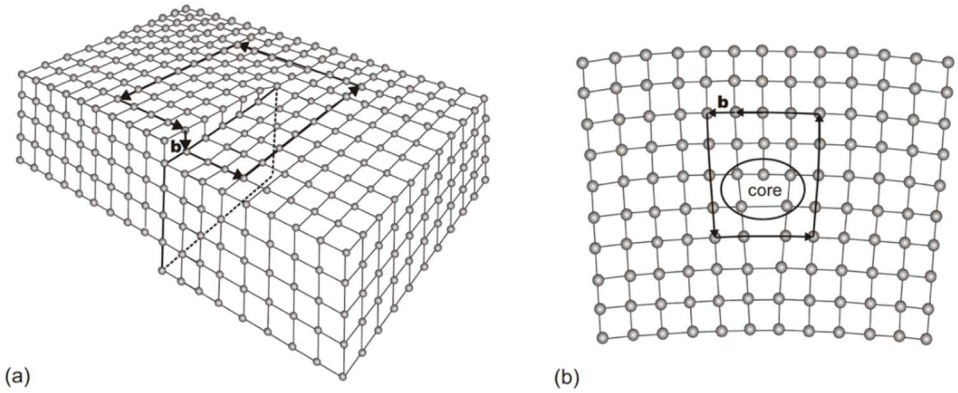

Figure 7: (a) Screw-type dislocation for which the Burgers vector **b** is parallel to the dislocation. (b) Edge-type dislocation with Burgers vector **b** perpendicular to the dislocation.

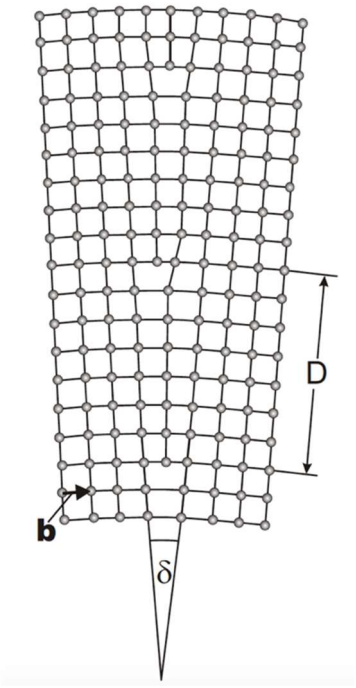

Figure 8: Grain boundary.

In this laboratory exercise we investigate ZnO samples heteroepitaxially grown on *c*-plane sapphire substrates. Sapphire can be seen to have a quasi-hexagonal lattice, that is to say the O-sublattice exhibits six-fold symmetry whereas the Al-sublattice has only a three-fold symmetry axis. The term *c*-plane means that the sapphire is cut parallel to its (0001) plane. The growth direction of ZnO on this substrate surface is the [0001] direction. In order to minimize the lattice mismatch, the ZnO lattice is rotated by 30° with respect to the sapphire substrate and thus forms a coincidence lattice therewith. Figure 9 illustrates the epitaxial relationship between the ZnO film and the sapphire substrate. But even then, the lattice mismatch $\Delta a/a$ = -18.4% is quite substantial. As a consequence, the critical layer thickness for pseudomorphical growth is less than one monolayer of ZnO. Therefore, the formation of dislocations, through which strain is released, starts with the very beginning of the film growth. This results in a columnar growth mode (Figure 10) with most of the dislocations perpendicular to the interface whereas there are few dislocations parallel to the interfacial plane. Hence, the vertical crystallite size is only limited by the layer thickness. The individual columnar crystallites are twisted and tilted with respect to one another. As we will see later, this causes a broadening of specific X-ray reflexes.

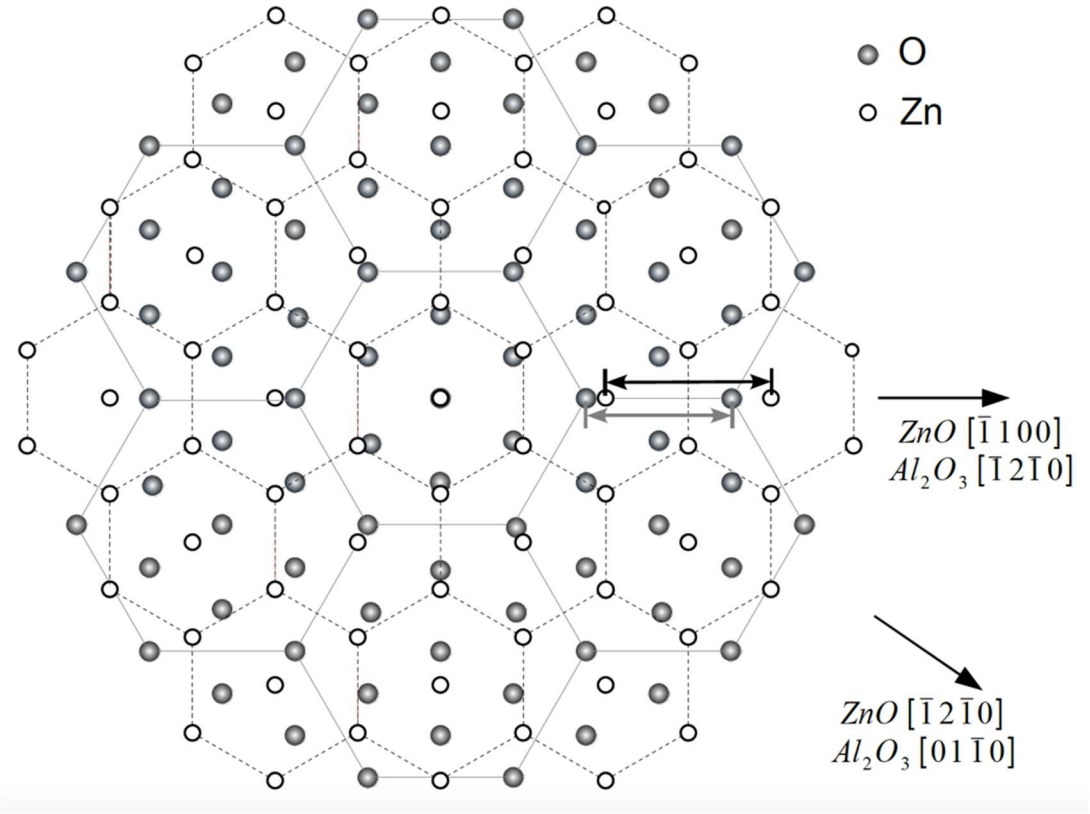

Figure 9: Formation of a coincidence lattice of the ZnO film and the sapphire substrate by a 30° rotation. For a clearer view, only the sapphire O-sublattice and the ZnO Zn-sublattice is depicted. The arrows indicate the distances which are relevant for the calculation of lattice mismatch.

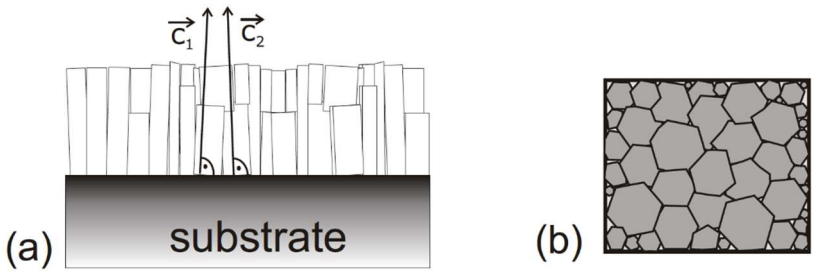

Figure 10: (a) Schematic side view of an epitaxial thin film showing the tilt of the crystallites. (b) Top view illustrating the twist.

However, the lattice mismatch between ZnO and $Zn_{1-x}Mg_xO$ layers is relatively small which allows pseudomorphical growth to take place. But the uppermost layer can also be partially relaxed or completely relaxed, depending on the layer thickness and the magnesium content *x* in the $Zn_{1-x}Mg_xO$ layer. For a quantitative analysis, the degree of relaxation *r*

$$r = \frac{a_{film} - a_{substrate}}{a_{film}^{relax} - a_{substrate}} \tag{5}$$

is defined, where a_{film} denotes the actually measured lattice constant of a thin film and a_{film}^{relax} the totally relaxed lattice constant. Thus, *r* is equal to 1 for fully relaxed films and equal to 0 for pseudomorphical growth.

2. Theory of X-ray Diffraction

In this section, we discuss the theory of X-ray diffraction. Though the dynamic theory in which the Maxwell equations are solved for a medium with a periodic and complex dielectric function is more accurate, it is perfectly sufficient to treat diffraction at real crystals with a mosaic structure within the less complex kinematic theory. The dynamic theory has to be only used for diffraction at ideal crystals. Since all the samples investigated in this laboratory exercise exhibit a mosaic structure, we constrain the discussion to the kinematic theory of X-ray diffraction.

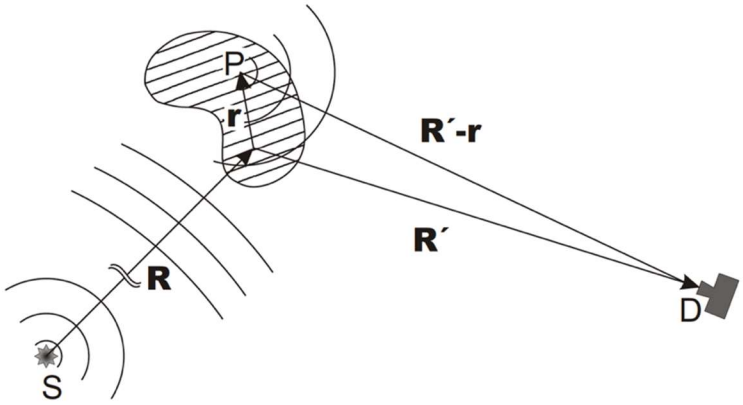

Figure 11: Schematic representation of the scattering process. D marks the position of the detector for which *R'* >> *r* is valid.

2.1. Kinetic Theory of X-ray Diffraction

The interaction between an electromagnetic wave and an atom can be described with an oscillator model. For large distances **R** between X-ray source and sample, the incident wave can be approximated by a plane wave whose electric field E_{in} is given by (Figure 11):

$$E_{in} = E_0 \cdot e^{i(\boldsymbol{k_{in}}\cdot(\boldsymbol{R}+\boldsymbol{r})-\omega_0 t)} \tag{6}$$

It induces harmonic oscillations of the shell electrons of an atom at point P and thus the emission of a spherical electromagnetic wave (Hertz dipole). This process is known as Thomson scattering. Given the fact that this is an elastic process, the scattered wave exhibits the same frequency and the same norm of the wave vector as the incident wave

$$|\boldsymbol{k_{in}}| = |\boldsymbol{k_{out}}| = |\boldsymbol{k}| = \frac{2\pi}{\lambda} \tag{7}$$

where λ denotes the X-ray wavelength. The amplitude of the scattered wave reads

$$E_{out} = f E_{in} \frac{e^{i\boldsymbol{k_{out}}\cdot(\boldsymbol{R'}-\boldsymbol{r})}}{|\boldsymbol{R'}-\boldsymbol{r}|} \tag{8}$$

Herein *f* denotes the scattering amplitude which depends on the type of atom and the frequency of the incident wave. At large distances from the scattering atom (*R'* >> *r*), the scattered wave can be approximated by a plane wave, and thus by inserting equation (6) into equation (8):

$$E_{out} = fE_0 \cdot e^{i(\boldsymbol{k_{in}}\cdot(\boldsymbol{R}+\boldsymbol{r})-\omega_0 t)} e^{i\boldsymbol{k_{out}}\cdot\boldsymbol{R'}} \frac{e^{-i\boldsymbol{k_{out}}\cdot\boldsymbol{r}}}{R'} \qquad (9)$$
$$= f\frac{E_0'}{R'} e^{i(\boldsymbol{k_{in}}-\boldsymbol{k_{out}})\cdot\boldsymbol{r}}$$

in which $E_0' = E_0 \cdot e^{i(\boldsymbol{k_{in}}\cdot\boldsymbol{R}+\boldsymbol{k_{out}}\cdot\boldsymbol{R'})} e^{-\omega_0 t}$.

The deduced expression (9) is valid for the scattering of a single atom. We now address the scattering of X-rays by an entire crystal. It is reasonable for the interaction between X-rays and solids to neglect multiple scatter processes (Born approximation). As a consequence, the scattered amplitude is proportional to the electron density *n*(**r**) of the crystal. Within the Frauenhofer approximation (*R'* >> *r*), all wave vectors $\mathbf{k_{out}}$ are parallel irrespective of the position P of the scattering atom. The scattered amplitude is then obtained by integrating over the whole crystal volume V:

$$E_{out} \propto \frac{E_0'}{R'} \int_V n(\boldsymbol{r}) e^{i(\boldsymbol{k_{in}}-\boldsymbol{k_{out}})\cdot\boldsymbol{r}} dV = \frac{E_0'}{R'} \int_V n(\boldsymbol{r}) e^{-i\boldsymbol{q}\cdot\boldsymbol{r}} dV \qquad (10)$$

In which we have defined the *scattering vector* **q**

$$\boldsymbol{q} = \boldsymbol{k_{out}} - \boldsymbol{k_{in}} \qquad (11)$$

Equation (10) shows that the amplitude of the scattered wave is proportional to the Fourier transformation of the electron density. By performing diffraction experiment, one cannot detect the amplitude but only the intensity I of the scattered wave, thus losing its phase information:

$$I \propto \frac{|E_0|^2}{R'^2} \left| \int_V n(\boldsymbol{r}) e^{-i\boldsymbol{q}\cdot\boldsymbol{r}} dV \right|^2 \qquad (12)$$

Therefore, the electron density cannot be simply obtained by an inverse Fourier transformation of the obtained diffraction pattern. Nevertheless, Equation (12) states the important result that the observed intensity is proportional to the modulus of the Fourier transformation of the scattering crystal lattice.

2.2. Reciprocal Lattice

Until now we made no use of the periodicity of the crystal. Yet, for a crystal the electron density n(**r**) has to be invariant under translations which constitute linear

combinations of lattice vectors $\boldsymbol{T} = u\boldsymbol{a_1} + v\boldsymbol{a_2} + w\boldsymbol{a_3}$ with *u*, *v*, *w* integer and $\mathbf{a}_i$ the fundamental lattice vectors. Hence,

$$n(\boldsymbol{r} + \boldsymbol{T}) = n(\boldsymbol{r}) \tag{13}$$

Periodic functions that satisfy Equation (13) can be expanded into a Fourier series. In one dimension the Fourier expansion reads

$$n(x) = \sum_m n_m e^{i(2\pi m/a)x} \tag{14}$$

The validity of equation (13) for a displacement of an arbitrary lattice vector $T_u = u\boldsymbol{a}$ can be easily verified. Likewise, in three dimensions the Fourier expansion is defined as

$$n(\boldsymbol{r}) = \sum_{\boldsymbol{G}} n_{\boldsymbol{G}} e^{i\boldsymbol{G}\cdot\boldsymbol{r}} \tag{15}$$

In order to satisfy Equation (13)

$$e^{i\boldsymbol{G}\cdot\boldsymbol{T}} = 1 \quad \forall\, \boldsymbol{T} \tag{16}$$

This involves

$$\boldsymbol{G}\cdot\boldsymbol{T} = 2\pi n \quad \forall\, \boldsymbol{T} \quad \wedge \quad n \text{ integer} \tag{17}$$

A suitable basis to construct vectors

$$\boldsymbol{G} = h\boldsymbol{b_1} + k\boldsymbol{b_2} + l\boldsymbol{b_3} \qquad \mathrm{h,k,l \text{ integers}} \tag{18}$$

that fulfills Equation (17) is given by:

$$\boldsymbol{b_1} = 2\pi\frac{\boldsymbol{a_2}\times\boldsymbol{a_3}}{\boldsymbol{a_1}(\boldsymbol{a_2}\times\boldsymbol{a_3})} \quad \boldsymbol{b_2} = 2\pi\frac{\boldsymbol{a_3}\times\boldsymbol{a_1}}{\boldsymbol{a_2}(\boldsymbol{a_3}\times\boldsymbol{a_1})} \quad \boldsymbol{b_3} = 2\pi\frac{\boldsymbol{a_1}\times\boldsymbol{a_2}}{\boldsymbol{a_3}(\boldsymbol{a_1}\times\boldsymbol{a_2})} \tag{19}$$

The vectors $\mathbf{b}_i$ and their linear combinations are referred to as *reciprocal lattice vectors*, because their dimension is m^{-1} and their length is inversely proportional to the length of the corresponding real lattice vectors. They span the so-called *reciprocal lattice*. It follows, that with every crystal structure there are two lattices associated, namely its space lattice in real space and its reciprocal lattice in Fourier space. The reciprocal lattice exhibits the same symmetries as the real crystal lattice. As both lattices are directly linked with each other via Equation (19), by determining properties of the reciprocal lattice one easily obtains the same properties of the space lattice. Also, by rotating or translating the space lattice the reciprocal lattice is also rotated or translated. One could readily verify that:

$$\boldsymbol{a_i}\cdot\boldsymbol{b_j} = 2\pi\delta_{ij} \tag{20}$$

and consequently, all reciprocal lattice vectors constructed according to Equation (18) satisfy Equation (17).

There is an important relation between the lattice planes of the crystal lattice and the reciprocal lattice vectors [1]: The reciprocal lattice vector $\boldsymbol{G_{hkl}} = h\boldsymbol{b_1} + k\boldsymbol{b_2} + l\boldsymbol{b_3}$ is perpendicular to the lattice planes with Miller indices (hkl) and the distance d_{hkl} between two such adjacent planes is given by

$$d_{hkl} = \frac{2\pi}{|\boldsymbol{G_{hkl}}|} \tag{21}$$

For a hexagonal lattice with lattice constant a and c this yields:

$$d_{hkl} = \frac{a}{\sqrt{\frac{4}{3}(h^2 + k^2 + hk) + \left(\frac{a}{c}\right)^2 l^2}} \tag{22}$$

2.3. X-ray Diffraction at Periodic Structures

We now insert the Fourier expansion of the electron density, according to Equation (15), into Equation (12):

$$I \propto \frac{|E_0|^2}{R'^2}\left|\sum_{\boldsymbol{G}} n_{\boldsymbol{G}} \int_V e^{i(\boldsymbol{G}-\boldsymbol{q})\cdot\boldsymbol{r}} dV\right|^2 \tag{23}$$

For a macroscopic crystal, whose side lengths l_x, l_y, and l_z are typically 10^7 – 10^8 times the lattice constants, the integral in equation (23) shows a δ-like behavior.

$$\begin{aligned}
\int_V e^{i(\boldsymbol{G}-\boldsymbol{q})\cdot\boldsymbol{r}} dV &= \left(\int_{\frac{-l_x}{2}}^{\frac{l_x}{2}} e^{i(G_1-q_1)\cdot x} dx\right)\cdot\left(\int_{\frac{-l_y}{2}}^{\frac{l_y}{2}} e^{i(G_2-q_2)\cdot y} dy\right)\cdot\left(\int_{\frac{-l_z}{2}}^{\frac{l_z}{2}} e^{i(G_3-q_3)\cdot z} dz\right) \\
&= \left(\frac{\sin\left(l_x\cdot\frac{1}{2}(G_1-q_1)\right)}{\frac{1}{2}(G_1-q_1)}\right)\cdot\left(\frac{\sin\left(l_y\cdot\frac{1}{2}(G_2-q_2)\right)}{\frac{1}{2}(G_2-q_2)}\right)\cdot\left(\frac{\sin\left(l_z\cdot\frac{1}{2}(G_3-q_3)\right)}{\frac{1}{2}(G_3-q_3)}\right) \\
&= \begin{cases} l_x l_y l_z = V & \text{for } \mathbf{q} = \mathbf{G} \\ \approx 0 & \text{otherwise} \end{cases} \qquad \text{for large } l_x, l_y, l_z
\end{aligned} \tag{24}$$

This can be interpreted the way that only if the *Laue condition*

$$\boldsymbol{q} = \boldsymbol{G} \tag{25}$$

is fulfilled, which states that only if the scattering vector is equal to a reciprocal lattice vector, an X-ray reflex can be observed. Because then the scattered X-rays interfere constructively along the direction of $\mathbf{k_{out}}$, that is to say the phase factors of the waves scattered at different lattice points of the crystal differ only by a factor $e^{2\pi n}$ (n integer) along $\mathbf{k_{out}}$. If the phase factor has a slightly different value than $e^{2\pi n}$, the contribution from the all lattice points average to

zero very effectively due to the high number of scatterers. Hence, for constructive interference relation Equation (23) yields for the intensity of the observed X-ray reflex:

$$I \propto \frac{|E_0|^2}{R'^2} \left| n_{\boldsymbol{G_q}} \right|^2 V^2 \tag{26}$$

Equation (26) expresses the important result that for coherent X-ray scattering the scattered intensity is proportional to V^2 and thus to N^2, where N denotes the number of lattice points.

2.4. Bragg Equation

We now try to give an intuitively clearer interpretation of the diffraction process. By inserting the diffraction condition (25) into Equation (21) and taking into account that $\boldsymbol{G} = n\boldsymbol{G_{hkl}}$ (n integer) one finds:

$$d_{hkl} = \frac{2\pi n}{|\boldsymbol{q}|} = \frac{2\pi n}{2\sin\theta \cdot \frac{2\pi}{\lambda}} \tag{27}$$

Herein 2θ represents the angle between incident and scattered waves (Figure 12(a)) and n the diffraction order. By rearranging this result, the famous *Bragg equation* can be obtained:

$$2d_{hkl}\sin\theta = n\lambda \tag{28}$$

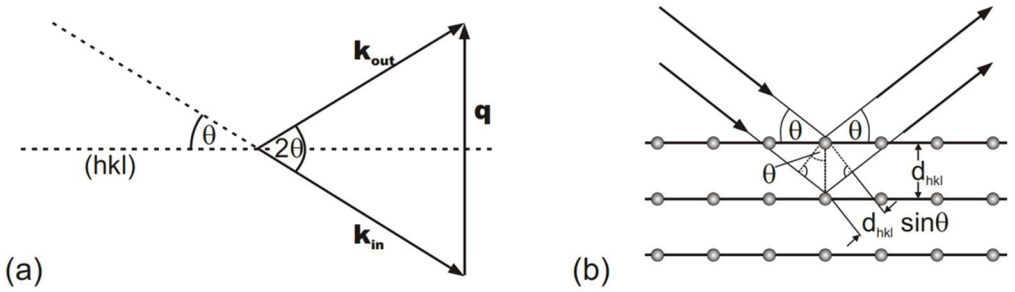

Figure 12: (a) The so-called scattering triangle. (b) Illustration of the Bragg equation.

The Bragg equation (28) has a simple interpretation (Figure 12(b)): The lattice planes (hkl) partially reflect the incident wave. The diffraction condition then amounts to the requirement that the path difference for waves reflected by adjacent lattice planes has to be an integer multiple of the wave length λ.

2.5. Ewald Sphere

In the last section we tried to get a deeper insight in the diffraction process by interpreting it more intuitively. We saw that the Bragg equation relates every X-ray reflex that can be observed with a set of parallel lattice planes (hkl). The Laue condition, however, assigns every X-ray reflex to a reciprocal lattice point. This makes it convenient to label the reflexes with the indices of their corresponding reciprocal lattice points HKL, as illustrated in

Figure 13: In the upper part, the $(H0L)$ plane of reciprocal space of a crystal with Wurtzite structure is displayed. According to Equation (11) and Figure 12(a), the maximum length of the scattering vector q_{max} in the case of backscattering (θ= 90°) is given by:

$$q_{max} = 2|\boldsymbol{k}| = \frac{4\pi}{\lambda} \tag{29}$$

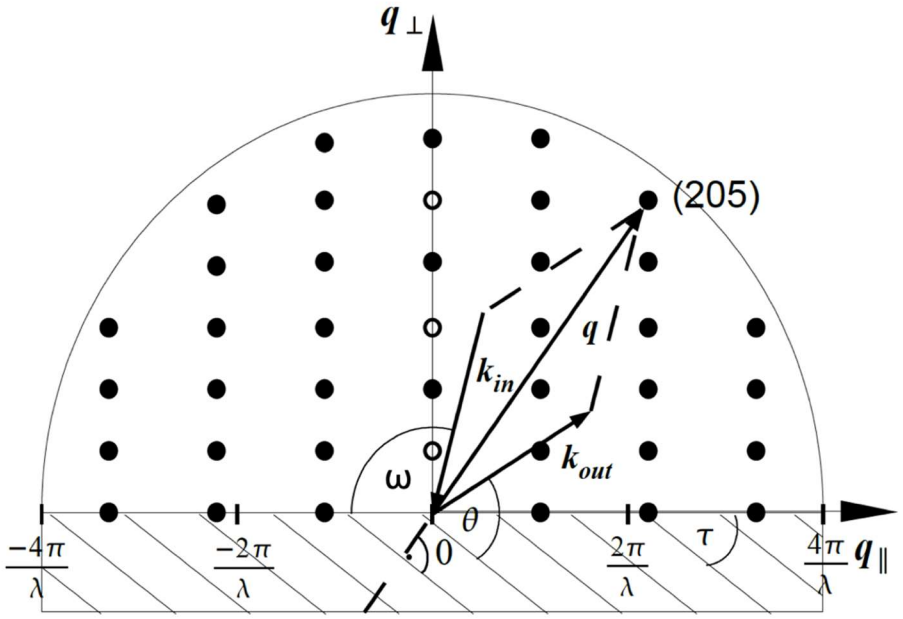

Figure 13: Ewald sphere.

Whenever the scattering vector is equal to a reciprocal lattice vector, an X-ray reflex is observed, as shown exemplarily for the (205) reflex. As a consequence, all reflexes which for a given wavelength λ are accessible for diffraction experiments are situated within the hemisphere with radius equal to $4\pi/\lambda$.

In the lower part of Figure 13, the lattice planes are depicted which scatter the incident X-ray beam according to the Bragg interpretation. ω designates the angle between the crystal surface and the incident X-ray beam, θ the angle between scattering lattice planes and incident X-ray beam and $\tau = \omega - \theta$ is the offset angle between crystal surface and scattering planes. The reflexes on the [001] axis, also labeled as $q_\perp$, are called symmetrical because for them $\omega = \theta$. All the other reflexes are called asymmetrical. The components of the scattering vector parallel $q_\parallel$ and perpendicular $q_\perp$ to the crystal surface expressed as a function of ω and 2θ read:

$$q_\parallel = \frac{2\pi}{\lambda}[\cos(2\theta - \omega) - \cos\omega] \tag{30}$$

$$q_\perp = \frac{2\pi}{\lambda}[\sin(2\theta - \omega) + \sin\omega] \tag{31}$$

2.6. Structure Factor

In Figure 13, the *(00L)* reflexes with *L* being odd numbers are represented by open circles, because these reflexes are forbidden, i.e. no scattered intensity is observed. In order to understand this, we now have to include the basis of the crystal lattice into our considerations. More generally, to be able to predict the intensity for different reflexes, we have to evaluate the Fourier coefficient $n_{\boldsymbol{G_q}}$ in Equation (26). $n_{\boldsymbol{G_q}}$ is related to $n(\mathbf{r})$ by:

$$n_{\boldsymbol{G_q}} = \frac{1}{V_{uc}} \int_{V_{uc}} n(\boldsymbol{r}) e^{-i\boldsymbol{G_q}\cdot\boldsymbol{r}} dV \tag{32}$$

which can be easily verified by inserting the Fourier expansion (15) of $n(\boldsymbol{r})$ into (32). The integration herein extends over the volume of the whole unit cell V_{uc}. In case the nuclei of the atoms are not too light, the principal contribution to the scattered X-ray intensity arises from the core electrons whereas the delocalized valence electrons can be neglected. Therefore $n(\mathbf{r})$ can be expressed as the sum over the electron densities $n_\alpha(\boldsymbol{\rho})$ of the various atoms of the unit cell:

$$n(\boldsymbol{r}) = \sum_{\alpha} n_\alpha(\boldsymbol{\rho}) \delta(r - r_\alpha) \tag{33}$$

where $\boldsymbol{\rho}$ denotes the distance from the center of a given atom α, and $\mathbf{r}_\alpha$ the position of an atom α with respect to the origin of the unit cell (Figure 14). With this Equation (32) can be rewritten as:

$$n_{\boldsymbol{G_q}} = \frac{1}{V_{uc}} \sum_{\alpha} e^{-i\boldsymbol{G_q}\cdot\boldsymbol{r_\alpha}} \underbrace{\int_{V_\alpha} n_\alpha(\boldsymbol{\rho}) e^{-i\boldsymbol{G_q}\cdot\boldsymbol{\rho}} dV}_{f_\alpha(\boldsymbol{G_q})} \tag{34}$$

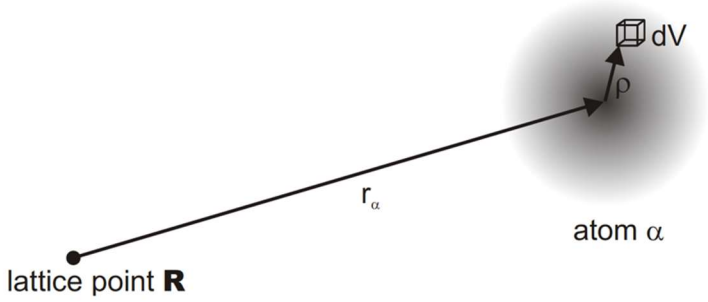

Figure 14: Definition of $\mathbf{r}_\alpha$ and $\boldsymbol{\rho}$. $\mathbf{r}_\alpha$ points the center of an atom α of the unit cell, $\boldsymbol{\rho}$ to a point with in that atom.

Now we integrate only over the volume V_α of a single atom, multiply the result with the appropriate phase factor and sum up over all the atoms of the unit cell. The *atomic scattering factor* $f_\alpha(\boldsymbol{G_q})$ defined in Equation (34) can be seen as the Fourier transformation of the atomic electron density. If the electrons were point charges at the atomic centers $\mathbf{r}_\alpha$,

$f_\alpha(\boldsymbol{G_q})$ = 1 independent of $\boldsymbol{G_q}$. But since the electron density in general stretches over some angstroms around $\mathbf{r}_\alpha$, $f_\alpha(\boldsymbol{G_q})$ is not constant but decreases for higher indexed reflexes. Accordingly, the Fourier coefficient $n_{\boldsymbol{G_q}}$ is also known as *structure factor* S_{HKL} ($\boldsymbol{G_q} = h\boldsymbol{b_1} + k\boldsymbol{b_2} + l\boldsymbol{b_3}$):

$$S_{HKL} = \sum_\alpha f_\alpha(\boldsymbol{G_q}) e^{-i\boldsymbol{G_q}\cdot\boldsymbol{r_\alpha}} \tag{35}$$

The position $\boldsymbol{r_\alpha} = u_\alpha \boldsymbol{a_1} + v_\alpha \boldsymbol{a_2} + w_\alpha \boldsymbol{a_3}$ of the atoms in the unit cell can be expressed by triples ($u_\alpha v_\alpha w_\alpha$) with u_α, v_α, w_α < 1. By taking into account Equation (20), the structure factor then reads:

$$S_{HKL} = \sum_\alpha f_\alpha(\boldsymbol{G_q})\, e^{-2\pi i(hu_\alpha + kv_\alpha + lw_\alpha)} \tag{36}$$

Finally, we want to evaluate the structure factor for the ideal Wurtzite lattice. The oxygen atoms in the unit cell are situated at (000), $\left(\frac{1}{3}\frac{2}{3}\frac{1}{2}\right)$, the zinc atoms at $\left(00\frac{3}{8}\right)$ and $\left(\frac{1}{3}\frac{2}{3}\frac{7}{8}\right)$ (Figure 3). Therefore, we obtain:

$$S_{HKL} = f_O\left(1 + e^{-2\pi i\left(\frac{h}{3}+\frac{2k}{3}+\frac{l}{2}\right)}\right) + f_{Zn}\left(e^{-2\pi i\frac{3l}{8}} + e^{-2\pi i\left(\frac{h}{3}+\frac{2k}{3}+\frac{7l}{8}\right)}\right) \tag{37}$$

We now examine the structure factors for the symmetric *00L* reflexes:

$$\begin{aligned} S_{00L} &= f_O\left(1 + e^{-i\pi l}\right) + f_{Zn}\left(e^{-i\pi\frac{3l}{4}} + e^{-i\pi\frac{7l}{4}}\right) \\ &= f_O\left(1 + (-1)^l\right) + f_{Zn}\left(e^{-i\pi\frac{3l}{4}} + (-1)^l e^{-i\pi\frac{3l}{4}}\right) \\ &= \begin{cases} 2\left(f_O + e^{-i\pi\frac{3l}{4}} f_{Zn}\right) & l\ even \\ 0 & l\ odd \end{cases} \end{aligned} \tag{38}$$

This shows that no intensity is observed for reflexes *(00L)* if *L* is any odd number. One can get a more intuitive picture by viewing the Wurtzite lattice as two interpenetrating, hexagonal close-packed lattices. Each of the sublattices has two atoms per unit cell at (000) and $\left(\frac{1}{3}\frac{2}{3}\frac{1}{2}\right)$. Therefore, d_{hkl} is effectively reduced by a factor of 2. When *L* is an odd number, the waves reflected at the centered lattice planes interfere destructively with the ones limiting the unit cell.

3. Experimental Setup

Figure 15(a) shows schematically the measurement configuration of *Rigaku SmartLab*, a high-resolution X-ray diffractometer. The X-ray source, which is a copper (Cu) cathode driven by 40 kV high voltage, generates the incident X-ray beam, then a monochromator is used for selecting the $Cu_{K\alpha 1}$ emission line ($\lambda = 1.54059\text{Å}$). The intensity of the diffracted beam can be measured by a CCD detector that is mounted on the same goniometer as the X-ray source. The angle between the incident X-ray beam and the sample surface is denoted as ω, while the angle enclosed by the incident beam and the diffracted beam is denoted as 2θ. An incident slit (IS) defines the size of incident X-ray beam, while the angular resolution of measurement can be adjusted by the two receiving slits (RS1 and RS2). In addition to the incident angle ω, sample rotation around the other two Euler angles – ϕ and χ – are controlled by the sample mounting stage (Figure 15(b)).

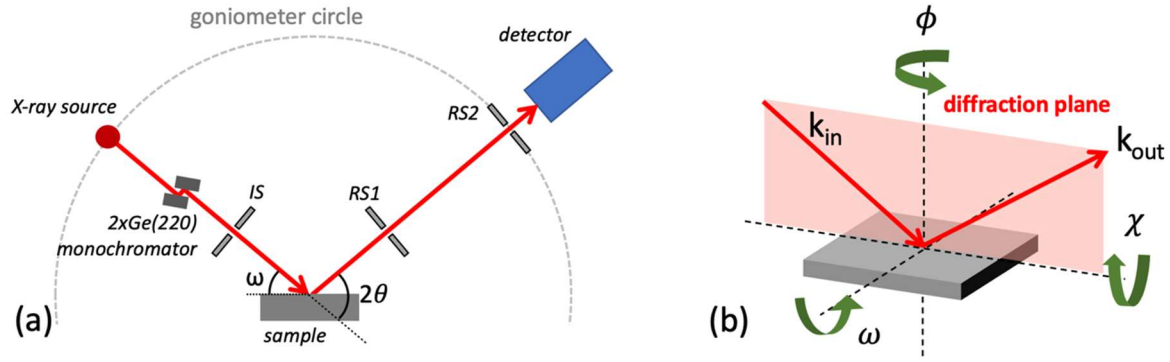

Figure 15: (a) Schematic diagram of HRXRD diffractometer. (b) Definition of the three sample rotation axes.

According to Equations (30) and (31), various scattering vectors can be measured by choosing different combinations of ω and 2θ. However, differentiating Equation (28) and subsequently dividing the result by the same Equation (28) yields the differential Bragg equation:

$$\frac{\Delta\lambda}{\lambda} = \cot\theta \cdot \Delta\theta + \frac{\Delta d_{hkl}}{d_{hkl}} \tag{39}$$

In order to accurately determine d_{hkl}, Equation (39) implies that not only good angular resolution is necessary, a highly monochromatic incident beam is also desirable. As shown in Figure 16, X-ray emission of Cu exhibits several characteristic wavelengths. These sharp and distinct emission lines – named $K\alpha_1$, $K\alpha_2$ and $K\beta$ – stem from radiative recombination from different atomic states. To reduce such wavelength dispersion, our HRXRD diffractometer utilizes a channel-cut germanium (Ge) single crystal on which the incident X-ray beam bounces twice off the (220) surfaces (Figure 15). At the correct angle only the $Cu_{K\alpha 1}$ emission

line remains; however, this comes at the expense of ~ 70% X-ray photon flux. Equation (39) also suggests that the $\Delta\theta$ term can be significantly suppressed when $\theta \to 90°$, meaning that higher indexed reflexes (e.g. (006) versus (004)) are preferable for determining lattice constants. However, it should also be noted that higher indexed reflexes typically exhibit weaker diffraction intensities.

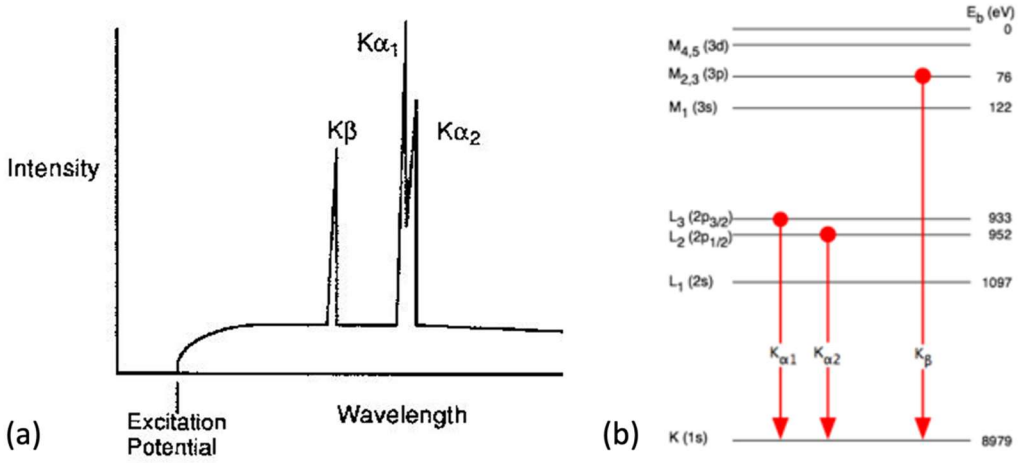

Figure 16: (a) X-ray emission spectrum of Cu. (b) Atomic transitions associated with Cu $K\alpha_1$, $K\alpha_2$ and $K\beta$ emission lines.

4. Characterization of Real Crystals by HRXRD

By means of HRXRD, deviations from the ideal crystal structure are investigated. For this purpose, the position and the width of X-ray reflexes are measured by registering the scattered X-ray intensity while rotating the sample around an Euler angle or changing the detector position and thus varying the length and the direction of the scattering vector. In Figure 17 the scattering geometry for a symmetrical and asymmetrical reflex is shown together with the scan directions of a $2\theta/\omega$- and an ω-scan.

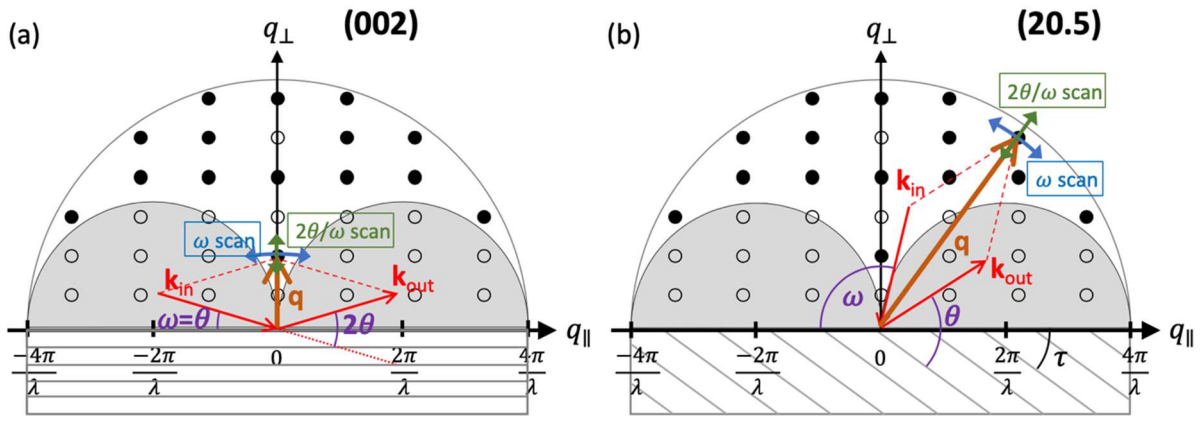

Figure 17: Ewald construction illustrating the scattering geometry in the case of a (a) symmetrical and an (b) asymmetrical reflex. The green and blue arrows show the scan directions for a $2\theta/\omega$-scan and an ω-scan, respectively. The reflexes within gray semicircles are in a conventional scattering geometry only accessible in transmission.

4.1. 2Theta-Omega Scan

By executing a $2\theta/\omega$-scan, the incident angle ω is increased by moving the X-ray source along the goniometer circle, while the detector rotates simultaneously with twice the angular velocity (Figure 15(a)). The direction at which the scattering vector is pointing thereby remains unchanged, only the length of the scattering vector is varied. For symmetrical reflexes $\omega = \theta$ and therefore the scan direction is along $q_\perp$ (Figure 17(a)). Particularly, this scan along $q_\perp$ is useful for checking if there are other crystalline phases incorporated in the crystal, which is true if other than the expected reflexes are observed. Moreover, the occurrence of forbidden reflexes hints at structural disorder in the examined crystal.

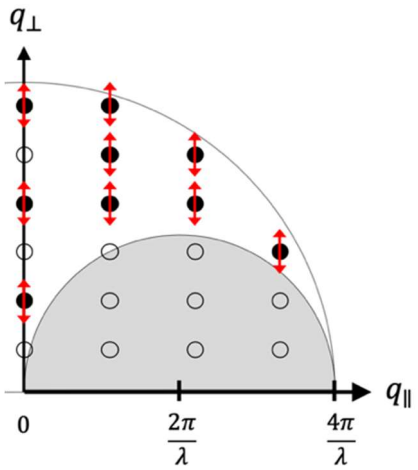

Figure 18: Broadening of the X-ray reflexes for a finite vertical coherence length. It is the same for all reflexes and solely determined by the film thickness l_z.

In this laboratory exercise, we investigate thin films grown on a substrate (Figure 10). The vertical coherence length, i.e. the length of the crystallites that scatter the incident X-ray beam coherently, is limited by the layer thickness. Consequently, the integral in Equation (24) is also non-zero for a scattering vector ***q*** slightly different from a reciprocal lattice vector ***G***:

$$I \propto \frac{|E_0|^2}{R'^2}\left|\sum_{\boldsymbol{G}} n_{\boldsymbol{G}} \int_V e^{i(\boldsymbol{G}-\boldsymbol{q})\cdot\boldsymbol{r}} dV\right|^2 = \frac{|E_0|^2}{R'^2}\left|n_{\boldsymbol{G_q}}\right|^2 l_x l_y \cdot \left|\frac{\sin(\Delta q_z l_z)}{\Delta q_z}\right|^2 \tag{40}$$

where we define $\frac{1}{2}(G_3 - q_3) = \Delta q_z$. Therefore, the measured X-ray diffraction peaks are not δ-like, but are broadened along the $q_\perp$ direction (Figure 18). The function $\frac{\sin^2(\Delta q_z l_z)}{(\Delta q_z)^2}$ is plotted in Figure 19. The full width at half maximum (FWHM) of the main maximum is proportional to $1/l_z$. The measured peak width $\Delta(2\theta)$ in [rad] of a symmetrical reflex can thus be correlated with the layer thickness [2]:

$$l_z = \frac{0.9\lambda}{\Delta(2\theta)\cdot\cos\theta} \tag{41}$$

Thereby we assumed that the broadening of the reflex along $q_\perp$ is only due to the finite coherence length, and other broadening mechanisms such as heterogeneous strain are neglected. Furthermore, besides the main peak, secondary maxima are observed when the numerator $|\sin(\Delta q_z l_z)|$ is maximum. The distance between such secondary maxima is $\Delta q_z^{max} = \frac{\pi}{l_z}$. From this it can be deduced for symmetrical reflexes that

$$l_z = \frac{\lambda\cdot\sin\theta}{\Delta\theta\cdot\sin 2\theta} \tag{42}$$

in which $\Delta\theta$ denotes half of the measured distance between secondary maxima in a $2\theta/\omega$-scan.

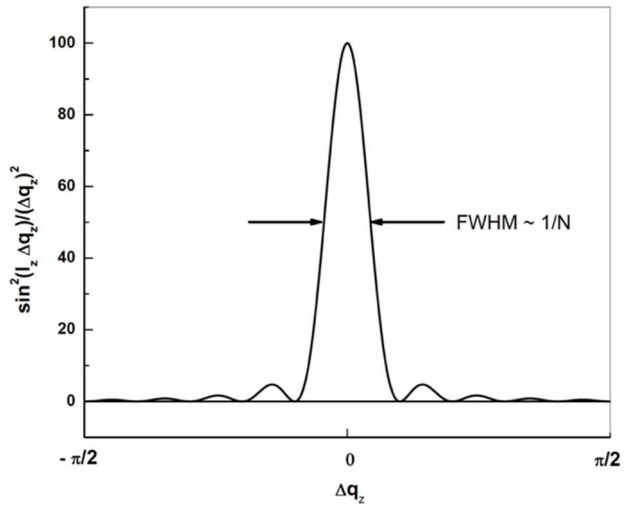

Figure 19: Plot of the function $\frac{\sin^2(\Delta q_z l_z)}{(\Delta q_z)^2}$ for $l_z = 10$. Its peak value is ${l_z}^2$, and its FWHM is proportional to $1/l_z$.

4.2. Omega Scan

By definition, in an ω-scan the sample is rotated around the ω-axis (Figure 15(b)) and the plot of the scattered X-ray intensity as a function of ω is often called the *rocking curve*. Practically, in our X-ray diffractometer this is done by keeping the sample fixed while scanning the X-ray source and detector concurrently toward the same direction, such that the incident angle ω is varied but 2θ remains unchanged. In the reciprocal space, an ω-scan entails a variation of the scattering vector on a circular path around the origin (Figure 17).

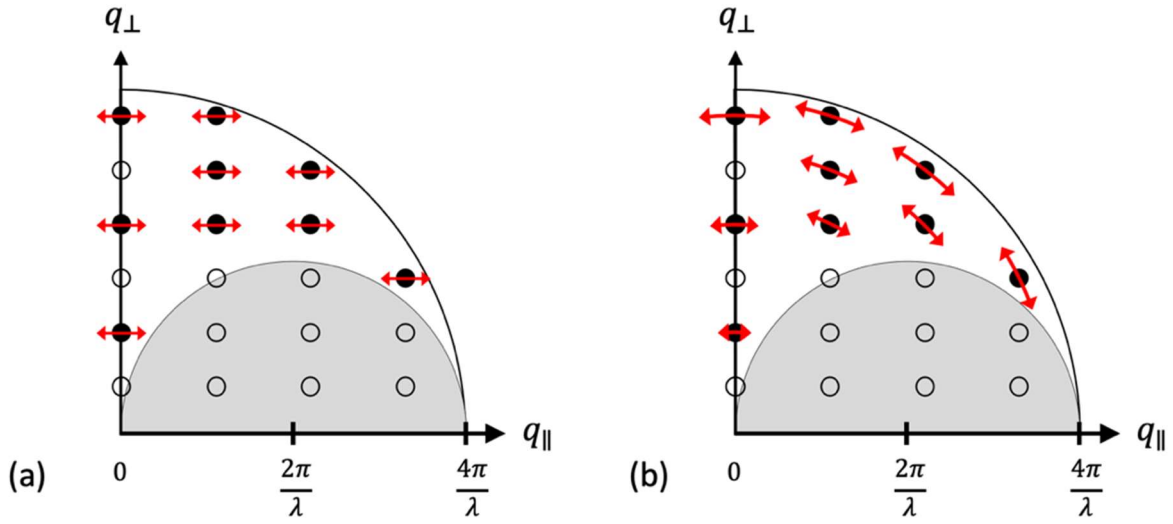

Figure 20: Broadening of the X-ray reflexes for a mosaic crystal. The finite coherence length in the growth plane gives rise to a broadening of the reflexes along $q_\parallel$, the tilt of the crystallites to a broadening along circular paths around the origin.

As discussed in section 1.2, the investigated ZnO films exhibit a columnar growth mode. Therefore, in the lateral plane perpendicular to the [0001]-direction the typical length for coherent scattering is limited by the crystallite size. This contributes to a broadening of the reflexes along the direction of limited coherence length, similar to the case of a finite layer thickness shown in Figure 18. For symmetrical reflexes the ω-scan direction is quasi parallel to this direction (Figure 20(a)). If one assumes that the limited coherence size is the only reason for the broadening of a symmetrical rocking curve, by determining its FWHM $\Delta\omega$ a lower limit for the lateral crystallite size $l_{\parallel}$ can be estimated by:

$$l_{\parallel} = \frac{0.9\lambda}{\Delta\omega \cdot \sin\theta} \tag{43}$$

However, a rocking curve of a symmetrical reflex in general is not exclusively broadened by a finite lateral coherence length, but also by the tilt of the crystallites (Figure 20(b)). This can be understood by examining Figure 21: For an ideal single crystal the Bragg equation (28) defines exactly the allowed angle of incidence for which a reflex can be observed. But a mosaic crystal is built up by many crystallites with different tilt angles $\delta\omega$ with respect to the [0001] direction. Thus, according to $\delta\omega$ the crystallites can be grouped in ensembles. By rotating the sample around the ω-axis, different ensembles are selected for which the Bragg equation (28) is fulfilled.

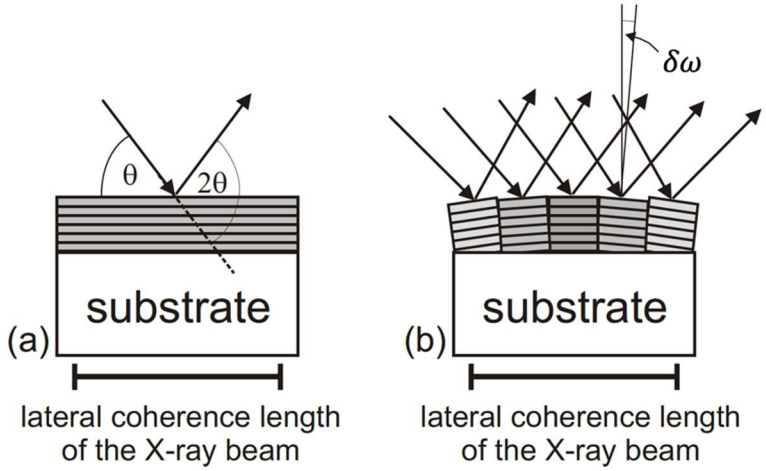

Figure 21: X-ray diffraction for a (a) ideal single crystal and (b) a mosaic crystal where the tilt of the crystallites with respect to one another broadens the rocking curve.

In conclusion, we have seen that the width of the rocking curve of a symmetrical reflex is influenced by a finite crystallite size as well as the tilt of the crystallites with respect to one another. Therefore, the FWHM $\Delta\omega_{002}$ of the (002) rocking curve is often used as a figure of merit to evaluate the degree of mosaicity of a thin epitaxial film. The smaller $\Delta\omega_{002}$, the better the individual crystallites are aligned and the larger their size are.

On the other hand, the twist of the crystallites (Figure 10(b)) in a mosaic crystal has no influence on the 002 rocking curve, because it produces no variation of the vertical position of the (0001) lattice planes. Instead, it can be seen as inducing a tilt of the $\{10\bar{1}0\}$ lattice planes. In order to investigate and quantify the twist of the crystallites, we thus have to determine the FWHM of the (100) rocking curve $\Delta\omega_{100}$. Yet, as the $\{10\bar{1}0\}$ planes of the investigated ZnO thin films are perpendicular to the substrate plane, the measurement of $\Delta\omega_{100}$ is not straightforward. One has to first determine the FWHM of rocking curves $\Delta\omega_{H0L}$ of which the associated lattice planes $\{h0\bar{h}l\}$ enclose successively smaller angles with the $\{10\bar{1}0\}$ lattice planes, then $\Delta\omega_{100}$ can be extrapolated. For this purpose, the measurements have to be conducted in a so-called pseudo-symmetrical *skewed geometry*, because in the conventional geometry the reflexes whose associated lattice planes enclose the smallest angles with the $\{10\bar{1}0\}$ lattice plane are not accessible (reflexes in the gray semicircles in Figure 17). In the conventional diffraction geometry, the offset angle τ of the asymmetrical lattice planes $\{h0\bar{h}l\}$ is compensated by an adjustment of the angle ω (Figure 22(a))). In the skewed geometry the sample is rotated by $\chi = \tau$ around the χ-axis in order to move the $\{h0\bar{h}l\}$ lattice planes in a position perpendicular to the diffraction plane that is defined by the direction of incident and scattered X-ray beam (Figure 22(b)(c)). Because τ is compensated by an adjustment of the Euler angle χ, this geometry is also called pseudo-symmetrical for its similarity to the symmetrical reflexes $\omega = \theta$.

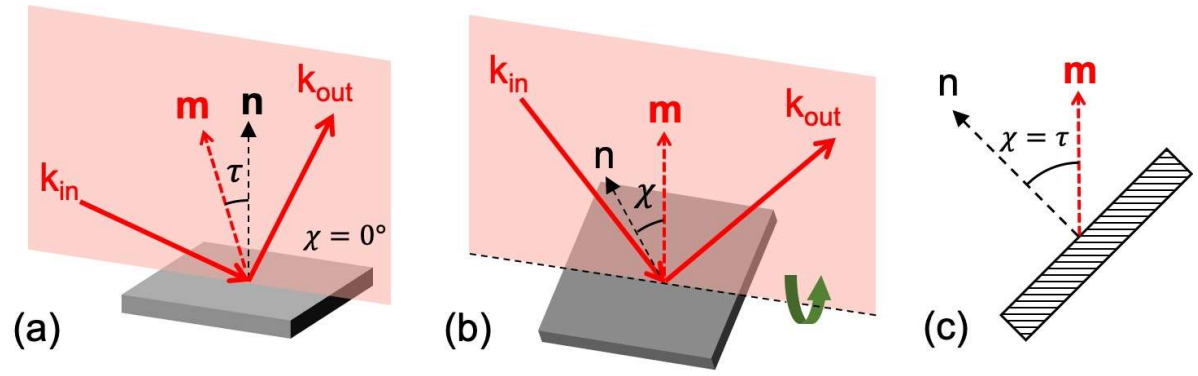

Figure 22: Illustration of the (a) conventional and (b) skewed geometry. For the conventional geometry the vector **n** normal to the sample surface and the vector **m** normal to the lattice plane lie in the diffraction plane. (c) In skewed geometry, **n** does not lie in the diffraction plane, but encloses an angle $\chi = \tau$ with it.

For a proper extrapolation, it is important that the FWHMs of the reflexes with a large angle χ can be determined. In order to extrapolate $\Delta\omega_{100}$, the measured $\Delta\omega_{H0L}$ are plotted as a function of χ and then fitted by:

$$\Delta\omega_{H0L} = \sqrt{(\Delta_0 \cos\chi)^2 + \left(\Delta_{\pi/2} \sin\chi\right)^2} \qquad (44)$$

where the fitting parameter Δ_0 corresponds to $\Delta\omega_{100}$. This is exemplarily shown in Figure 23. As this procedure is rather time-consuming, it is common to settle for approximating $\Delta\omega_{100}$ with the FWHM of the (101) rocking curve $\Delta\omega_{101}$ which can be directly measured. The reflex 201 would be better suited for this purpose, but it is often difficult to measure for thin films because of its low intensity. Figure 23 shows that $\Delta\omega_{101} = 0.35°$ and the extrapolated value $\Delta\omega_{100} = 0.4°$ differ only by 12.5%. Therefore, in order to study tendencies for samples grown under different growth conditions, the above approximation is quite reasonable. In section 1.2 we have seen that the tilt of the crystallites is due to screw-type dislocations whereas the twist is due to edge-type dislocation. Hence, by assuming that the broadening of the rocking curves originates only from tilt and twist, it is possible to calculate from the FWHMs $\Delta\omega_{002}$ and $\Delta\omega_{100}$ the dislocation densities by using the relations deduced by Dunn and Kogh [3]:

$$\rho_{screw} = \frac{\Delta\omega_{002}^2}{4.35 \cdot |\boldsymbol{b}_{screw}|^2} \tag{45}$$

$$\rho_{edge} = \frac{\Delta\omega_{101}^2}{4.35 \cdot |\boldsymbol{b}_{edge}|^2} \tag{46}$$

with the Burgers vector $\mathbf{b}_{\text{screw}} = [0001]$ for screw-type dislocations and $\mathbf{b}_{\text{edge}} = \frac{1}{3}[11\bar{2}0]$ for edge-type dislocations.

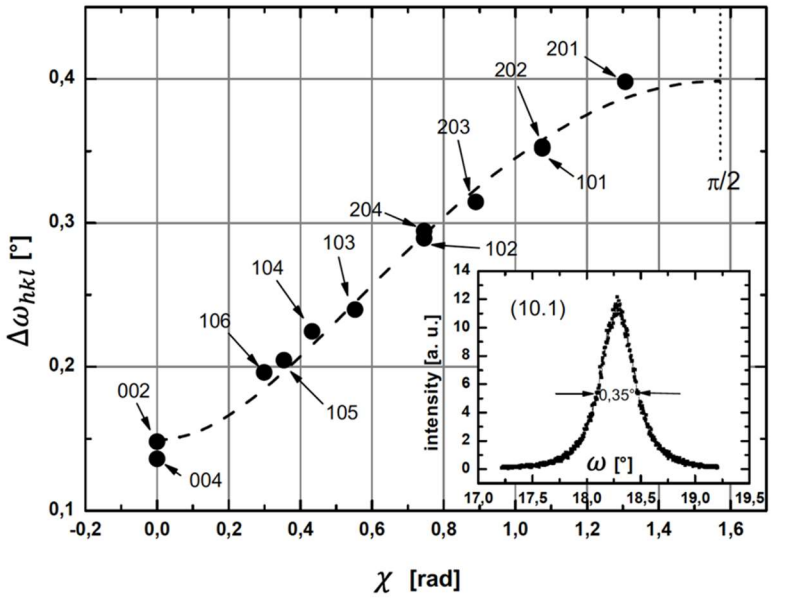

Figure 23: Measured FWHMs of rocking curves as a function of the angle fitted by Equation (44). In the inset the (101) rocking curve is shown.

4.3. Reciprocal Space Map

The scan mode mapping a two-dimensional region of reciprocal space is known as reciprocal space map. With a point (0D) X-ray detector, such a scan can be carried out by combining the $2\theta/\omega$- and the ω-scan mode in the following way: first for a given length of the scattering angle, an ω-scan is performed, then the $2\theta/\omega$-scan mode is employed to change the length of the scattering vector by a small amount δq, then again an ω-scan is performed and so on . . . In this exercise, the CCD X-ray detector of *Rigaku SmartLab* can be operated as an array (1D) detector, meaning that the diffraction intensities within an angular range of 2θ can be measured simultaneously. By scanning the ω steps, the reciprocal space map can be acquired in a much shorter time. The result of such a scan conducted at the position of the ZnO (205) reflex is shown in Figure 24. The arrows denote the peak broadening directions due to a finite lateral crystallite size and due to the tilt of the crystallites (mosaicity). The broadening due to the finite layer thickness can be neglected. Without using additional crystal analyzer, the instrument resolution is not sufficient for resolving these two principal broadening mechanisms, which is why the peak exhibits an ellipsoidal form. From the position of the principal axis it can be deduced that the broadening is due to both mechanisms.

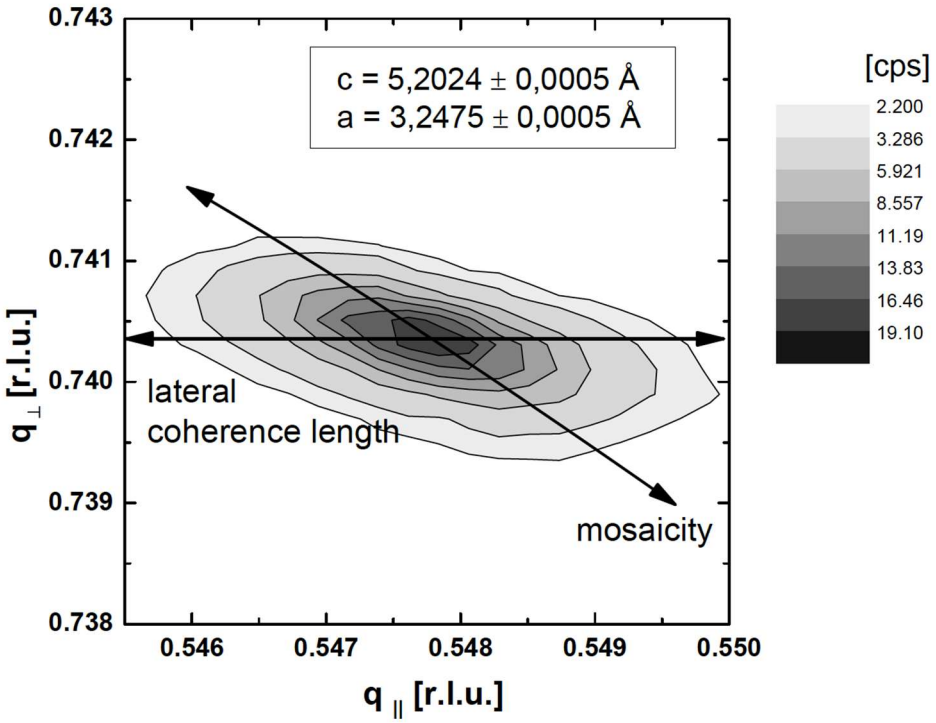

Figure 24: Reciprocal space map of the (205) reflex of a ZnO thin film. In the inset the calculated lattice constants are given.

A reciprocal space map of an asymmetrical reflex allows the determination of both the *a* and the *c* lattice constant. As discussed in section 3, the high indexed reflexes are best suited for this because the contribution of the limited angular resolution in Equation (39) decreases with θ. *a* and *c* can be calculated by determining the components $q_\perp$ and $q_\parallel$ of the peak center:

$$a = \frac{1}{q_\parallel(rlu)} \frac{\lambda}{\sqrt{3}} h \tag{47}$$

$$c = \frac{1}{q_\perp(rlu)} \frac{\lambda}{2} l \tag{48}$$

In the above equations $q_\perp$ and $q_\parallel$ have to be inserted in reciprocal lattice units (rlu), i.e. in units of $4\pi/\lambda$ which is equivalent to normalizing the radius of the Ewald sphere to 1.

4.4. Phi Scan

By performing a φ-scan, ω and 2θ are kept constant while the sample is rotated around the φ-axis. For our samples this corresponds to a rotation around the [0001]-axis. Hence, for asymmetric reflexes HKL, by performing a φ-scan of 360°, six peaks can be observed which is in accordance with the six-fold symmetry of the [0001]-axis. By conducting such a 360° φ-scan for the substrate and the thin film on top, the epitaxial relationship between substrate and thin film can be established.

5. Pre-Measurement Exercises

- Calculate the angle 2θ for the (002) reflex of ZnO, given that the X-ray wavelength $\lambda = 1.54059\text{Å}$ and the lattice constants of ZnO are c_{ZnO} = 5.20 Å, a_{ZnO} = 3.25 Å.
- Starting with Equation (21), derive Equation (22).
- Calculate $d_{10.1}$ – the distance of the $(10\bar{1}1)$ lattice planes. Calculate the offset angle τ of these lattice planes with respect to the (0001) lattice planes.

6. Experimental Procedure

In this experiment exercise, you will measure three samples in total. Among which, Sample A and B are ZnO thin films, while Sample C is a $Zn_{1-x}Mg_xO$ thin film. All samples were grown by molecular beam epitaxy (MBE) on sapphire (0001) substrates. To finish this exercise efficiently, it is recommended to carry out all measurements on a sample before moving to the next one, with the following sequence.

6.1. Optics Alignment

Before this experiment exercise starts, your instructor should have switched on the *Rigaku SmartLab* diffractometer and have the correct X-ray optics installed. ***You should not replace any X-ray optics*, other than the height reference sample plate, central slit, 4-inch wafer sample plate and the samples.** Please check the X-ray generator status at the bottom right corner, and ensure that it is operating at 40 kV and 50 mA, before continuing on the following steps. Otherwise, inform your instructor immediately.

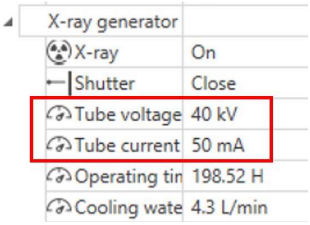

a) From **Part Activities** panel, double-click **Alignment Activity / Optics Alignment (PB)** to add it to the **Sequence** panel. Repeat the same for **Alignment Activity / Sample Alignment (Thin Film)** and **Measurement Activity / General Measurement**.

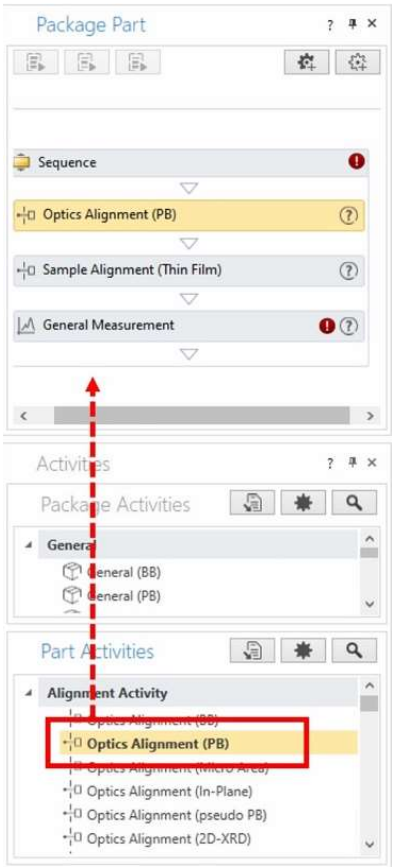

b) Click the 'Optics Alignment (PB)' tab in the sequence panel to display the setting dialog box. Select **'Customized optics'** then click on **'Customized…'**. In the new window, first click on **'Set Current Optics'** then check whether the optical part list is identical to the setting in the blue box below. Click on **'OK'** to proceed.

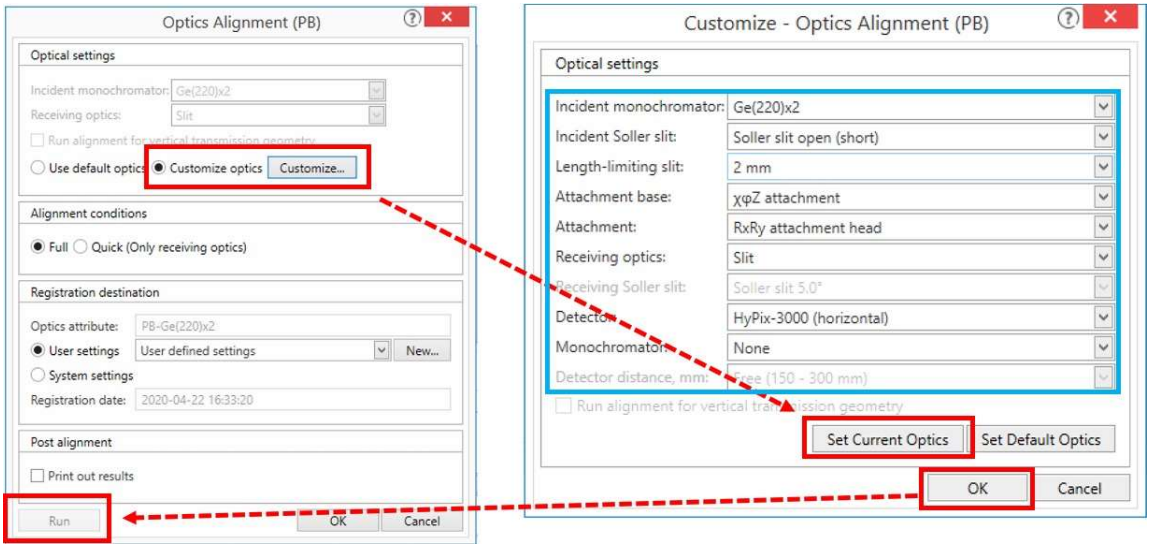

c) Click **'Run'** to execute the 'Optics Alignment (PB)' macro script. A window will pop up in ~ 15 seconds reminding the installation of alignment slit. Because this is already done by the instructor, click 'OK' to continue.

d) The diffractometer will align each optical component by maximizing the detected X-ray intensity going through the central slit. This process will take ~ 5 minutes.

6.2. Sample A Alignment

a) Click the 'Sample Alignment (Thin Film)' tab in the sequence panel to display the settings dialog box. Input the estimated sample dimensions. Ensure to select **'RxRy attachment head + 4-inch wafer sample plate'** and uncheck the 'Surface normal alignment' option.

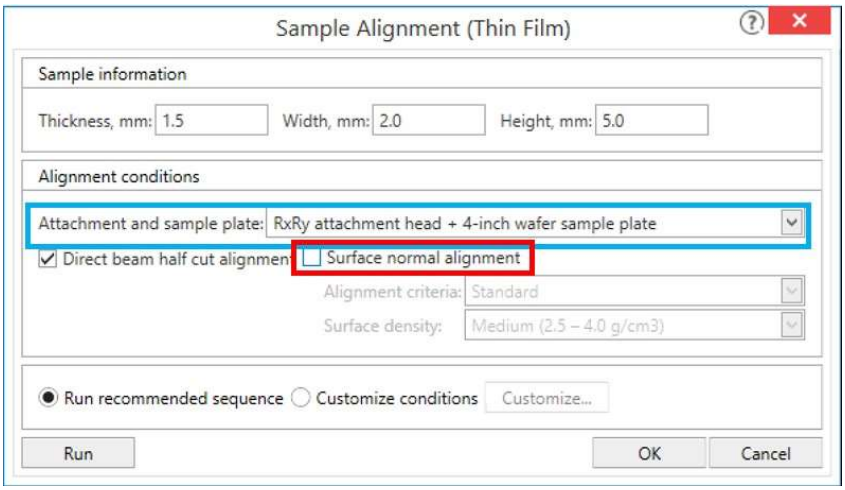

b) Click **'Run'** to execute the 'Sample Alignment (Thin Film)' macro script. A window with graphic instructions will pop up in ~ 15 seconds. Remove the central slit used for alignment. Press the gray lever on the back side of the height reference sample plate, then rotate it counter-clockwise to remove it.

c) Install the 0-3 mm spacer by aligning the latches with the corresponding holes, then securing it by rotating clockwise. Install the 4-inch wafer sample plate in the same way.

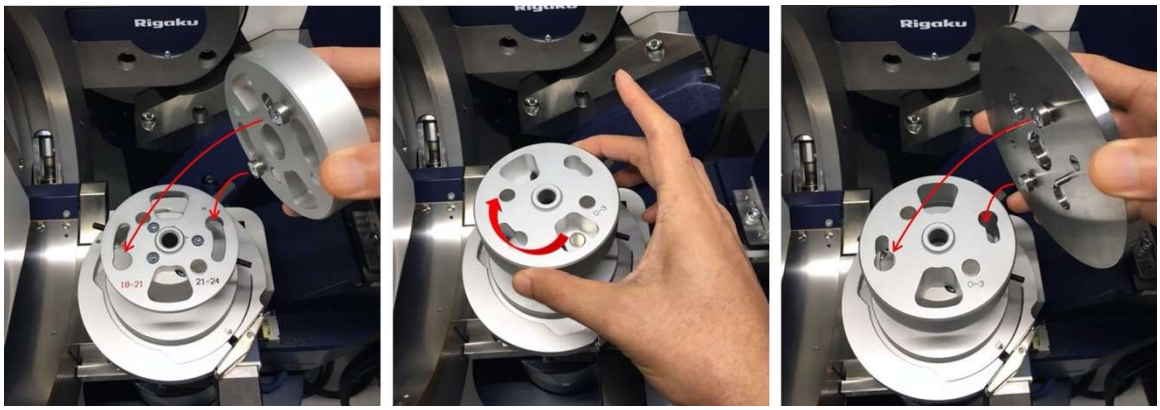

d) Use double-side tape to fix Sample A at the center of the sample holder. *The long side of sample should point toward the doors of diffractometer*.

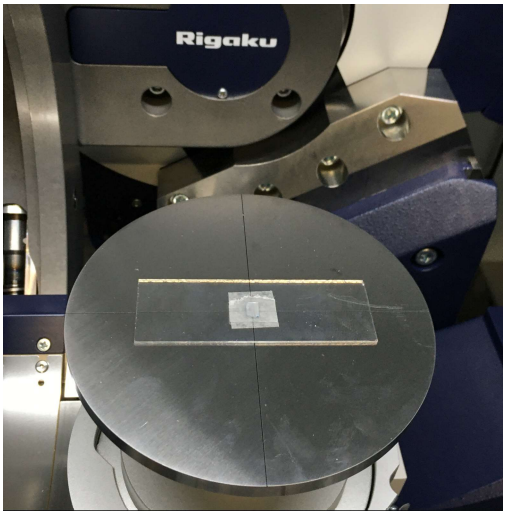

e) Click 'OK' in the instruction window. The script will vary the sample height (*Z* axis) and find the location at which the X-ray intensity is cut to exactly half of the maximum value. Then, an ω-scan finds the paralleling between the sample surface and the X-ray beam. The sequence repeats for three iterations, and the entire process will take ~ 2 minutes. At the end, find the *Z* value shown in the 'H/W Status' panel on the right-hand side, record the value in the measurement report sheets in Appendix A.

6.3. Sample A

Mosaicity of heteroepitaxial ZnO thin film – Rocking curve of the (002) reflex

a) First, perform alignment optimization to the symmetric ZnO (002) reflex. You can find the 2θ value for the ZnO (002) reflex in Appendix B. In the **Pro Control** panel (bottom of the software screen), move the $\theta/2\theta$-axis to this value. Observe how the X-ray source and detector move in the diffractometer. Check the 'H/W Status' panel – What is the value of ω-axis now? Record the $\theta/2\theta$ value in the measurement report sheets in Appendix A.

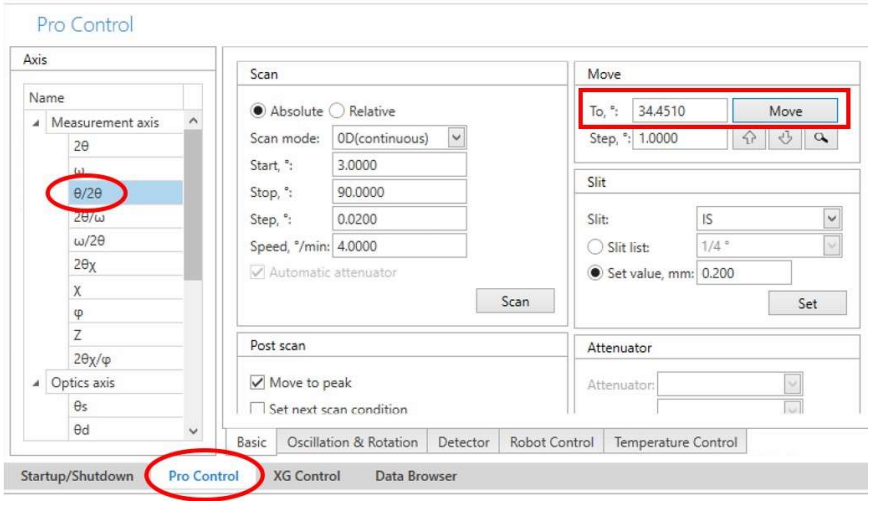

b) In the 'H/W Status' panel, check if the incident slit (IS) and the two receiving slits (RS1, RS2) are set at 1, 1, and 1.1 mm, respectively. If not, use the Slit setting box in the Pro Control window to adjust them.

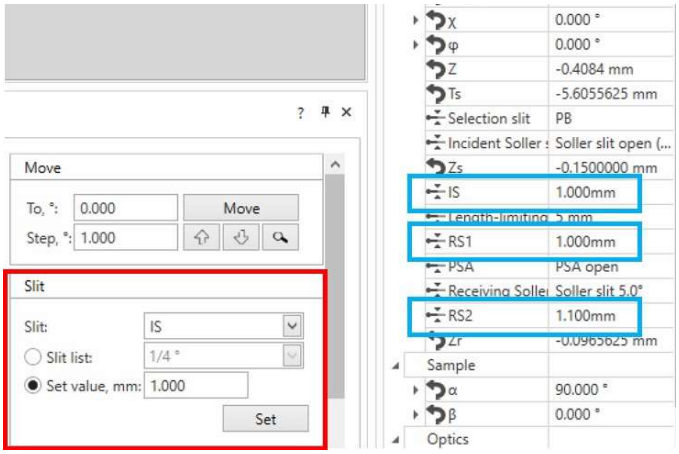

c) In Pro Control, select the ***φ*-axis** and set the scan type to **absolute, range to 0-360°, 1° step, and 180°/min speed**. Select the 'Move to peak' box below, then start the scan. Observe how the sample is moved during the scan.

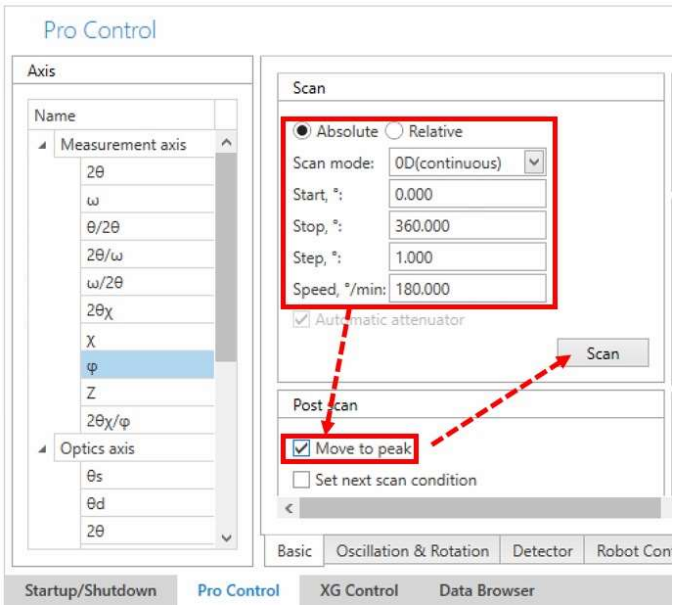

d) Due to the imperfect mounting of the sample on the wafer sample plate, this φ-scan should observe one or two broad peaks. After the scan, the software should automatically find the peak position and move the φ-axis there. (If the peak position assigned by the software is incorrect, select the 'Data Browser' tab on the top of control software, then 'Search Peaks → Full Width at Half Maximum Center.' Move the φ-axis to the new peak value by *Pro Control*.) Find the final φ position in the 'H/W Status' and record it to Appendix A.

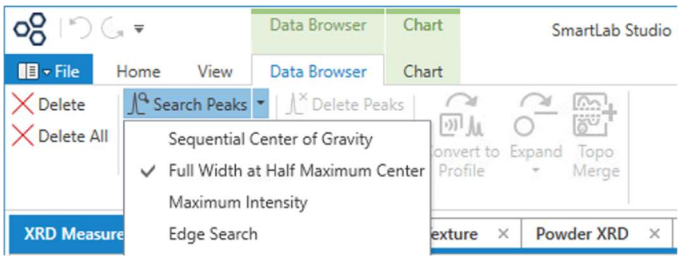

e) Now the imperfect sample mounting needs to be compensated by the ω-axis. To achieve this, switch to the ω-axis in Pro Control, set the scan range to **relative ±1°, 0.02° step, and 1°/min speed**. Observe how the ω- and 2θ-axes change in the 'H/W Status' panel. Record the optimized ω position.

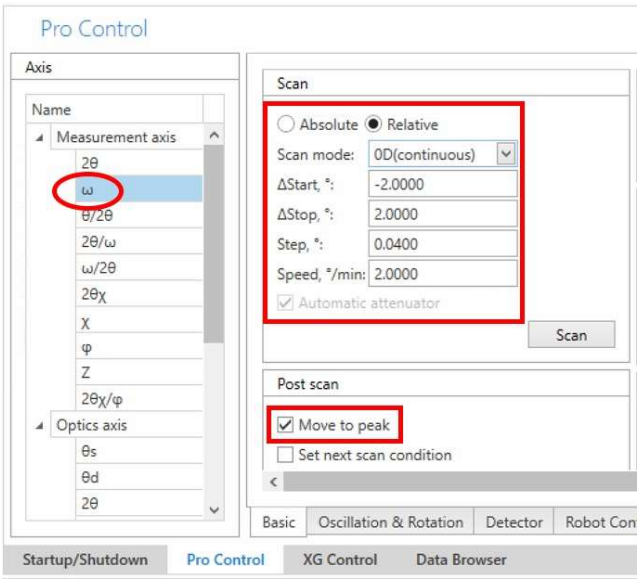

f) Change the slit setting to IS=0.05 mm, RS1=0.05 mm, and RS2=0.3 mm. Switch to $2\theta/\omega$ axis and set the scan range to relative $\pm 0.5°$, 0.01° step, and 0.5°/min speed. Observe how the ω- and $2\theta/\omega$-axes changes in the 'H/W Status' panel.' Record the optimized $2\theta/\omega$ position.

g) Now the actual rocking curve measurement (ω-scan) is performed on the ZnO (002) reflex. Click on the **'General Measurement'** tab established earlier in the sequence panel. Set up an ω-scan with a relative $\pm 0.5°$ range, 0.01° step, and 0.5°/min speed. Also change the slit setting to IS=0.05 mm, RS1=0.05 mm, and RS2=0.3 mm. In the 'File name:' field, choose an appropriate data folder and assign a name for this measurement (save the file in .RASX format). Click 'Run' to start the measurement. (You can drag this window sideways in order to follow the measurement progress.)

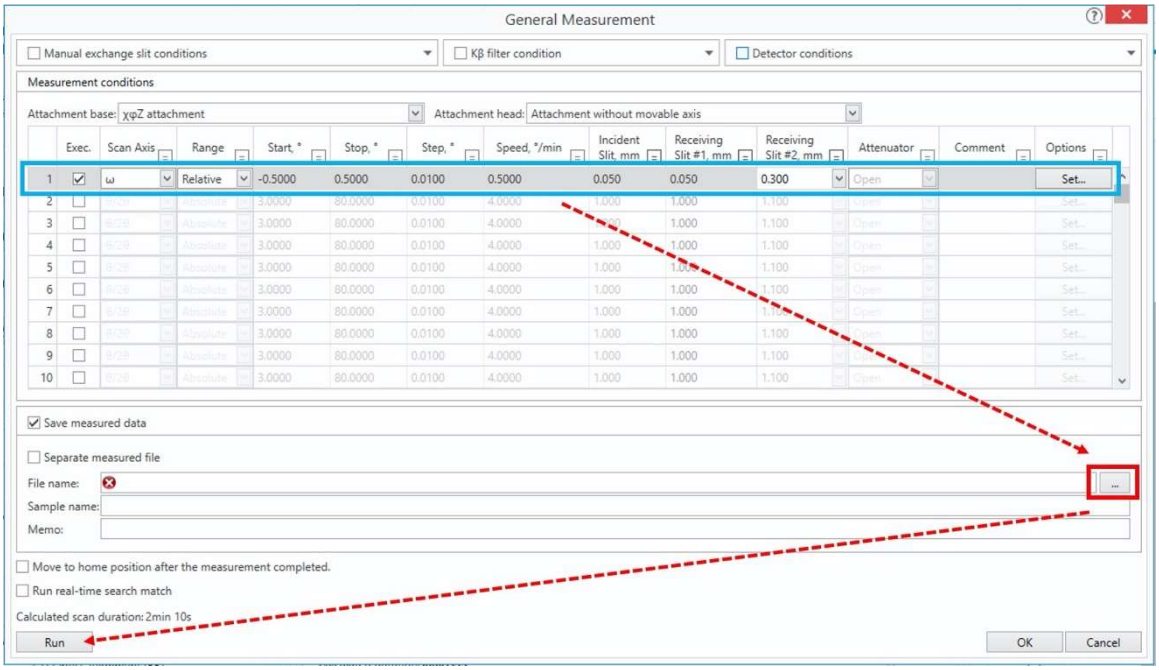

h) Close the 'General Measurement' window. On the top of control software, find the 'Data Browser' tab and then 'Search Peaks → Full Width at Half Maximum Center.' Record this peak value of ω-scan in Appendix A. To save the file in the .xy format for writing your lab report, go to the 'Data Browser' tab at the bottom, find the correct file under 'Package/ω/' and right click to select 'Export → Data To File.' Choose the .XY format as the file type.

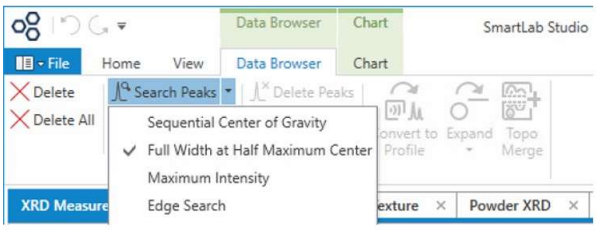

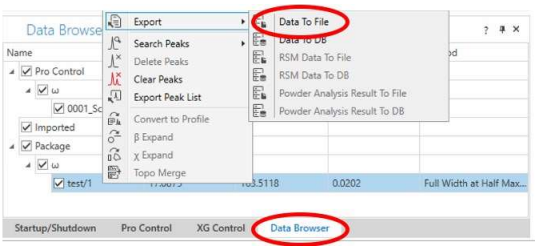

i) Now, use Pro Control to move the ω-axis to the new peak value that you just obtained from the ZnO (002) rocking curve measurement. Double check if both the ω- and $2\theta/\omega$-axes are at the right optimized values in the 'H/W Status' panel. Set up a $2\theta/\omega$-scan using 'General Measurement,' with a relative $\pm 0.2°$ range, 0.004° step, and 0.2°/min speed as described in part g). Search the peak position and export the data to .XY format as described in part h).

j) In the record tables of Appendix A, the measurements enclosed by thicker borders should be performed by the **'General Measurement'** function, and results should be saved. For all the prior measurements, the **'Pro Control'** function should be used.

Rocking curve of the ZnO (101) reflex

k) The next measurement will be the rocking curve of the ZnO (101) reflex, performed at the skewed geometry (see Figure 22(b)). Using 'Pro Control', move the $\theta/2\theta$-axis to the value of ZnO (101) reflex (use Appendix B). Then set the Euler angle χ to the offset angle τ of ZnO (101). Observe the movement of the sample. Change the slit settings to IS=1 mm, RS1=1 mm, and RS2=1.1 mm.

l) In 'Pro Control,' perform a φ-scan with 0-360° absolute range, 1° step, and 180°/min speed. Check if the peak value is assigned correctly (if not, manually search and move it). Record the new φ position afterwards.

m) Redo φ-scan but with a relative $\pm 2°$ range, 0.04° step, and 2°/min speed. Record the optimized φ position after the scan.

n) Still in 'Pro Control,' perform a χ-scan with a relative $\pm 2°$ range, 0.04° step, and 2°/min speed. Record the optimized χ position after the scan.

o) Optimize the ω-axis with a scan of relative $\pm 2°$ range, 0.04° step, and 2°/min speed. Record the optimized ω position after the scan.

p) Reduce the slit opening sizes to IS=0.2 mm, RS1=0.2 mm, and RS2=0.3 mm. In 'Prop Control,' perform a $2\theta/\omega$-scan with a relative $\pm 1.5°$ range, 0.03° step, and 1.5°/min speed. Record the optimized $2\theta/\omega$ position after the scan.

q) Using the 'General Measurement' function, set up and save an ω-scan with a relative $\pm 1.5°$ range, 0.03° step, and 1.5°/min speed. Set the slit opening sizes to IS=0.2 mm, RS1=0.2 mm, and RS2=0.3 mm. Search the peak position and export the data to .XY format as described in part h).

Epitaxial relationship between ZnO and Al_2O_3

r) Next we will confirm the epitaxial relationship between the ZnO layer and the sapphire substrate by performing two separate φ-scans on the ZnO (112) and Al_2O_3 (113) reflexes (absolute range 0-360°). These two scans will be done at skewed geometry ($\chi = \tau$), and you can find the relevant $\theta/2\theta$ and τ values in Appendix B. Use the slit settings of IS=1 mm, RS1=1 mm, and RS2=1.1 mm. Save and export the scan results properly.

6.4. Sample B

Mosaicity of heteroepitaxial ZnO thin film – Rocking curve of the (002) reflex

a) Install Sample B onto the sample holder. (If the instrument doors are locked, they can be unlocked by clicking on the 'Door Lock off' icon on the top task bar.) Follow the same sample alignment procedure as described in section 6.2. Record the sample height *Z* value after the alignment.

b) We will first perform a ZnO (002) rocking curve measurement, as was done for Sample A. However, the peak widths measured from Sample B should be substantially smaller, and the peak intensities substantially higher. Similar to steps a-c in section 6.3, use 'Pro Control' to move the $\theta/2\theta$-axis to the expected value for ZnO (002) reflex, then do a φ-scan with 0-360° absolute range, 1° step, and 180°/min speed. Record the optimized φ position after the scan.

c) Similarly, we now proceed with the optimization of the ω- and $2\theta/\omega$-axes. Use 'Pro Control' for an ω-scan with a relative $\pm 0.5°$ range, 0.005° step, and 0.5°/min speed. Record the new ω position.

d) Perform a $2\theta/\omega$-scan with a relative $\pm 0.5°$ range, 0.005° step, and 0.5°/min speed. Record the new $2\theta/\omega$ position.

e) Reduce the slit opening sizes to IS=0.05 mm, RS1=0.05 mm, and RS2=0.3 mm. Perform an ω-scan with a relative $\pm 0.2°$ range, 0.002° step, and 0.2°/min speed. Record the new ω position.

f) Perform another $2\theta/\omega$ optimization scan with a relative $\pm 0.3°$ range, 0.002° step, and 0.3°/min speed. Record the new $2\theta/\omega$ position.

g) Use the 'General Measurement' function to set up an ω-scan with a relative $\pm 0.05°$ range, 0.0002° step, and 0.05°/min speed. Search for the peak position, move to the new ω peak position by 'Pro Control,' and export the file to .XY format.

h) Use the 'General Measurement' function to set up a $2\theta/\omega$-scan with a relative $\pm 0.5°$ range, 0.001° step, and 0.2°/min speed. Search for the peak position and export the file to .XY format.

Wide range characterization of ZnO/Al_2O_3

i) Record a wide range $2\theta/\omega$-scan as shown in the figure below. Change the slit setting to IS=1 mm, RS1=1 mm, and RS2=1.1 mm. Set the scan range to be 20 – 150°, 0.2° step, and 5°/min speed. Export the data to .XY format for writing your lab report. (This scan takes ~ 26 minutes and you can schedule your lunch break during this time.)

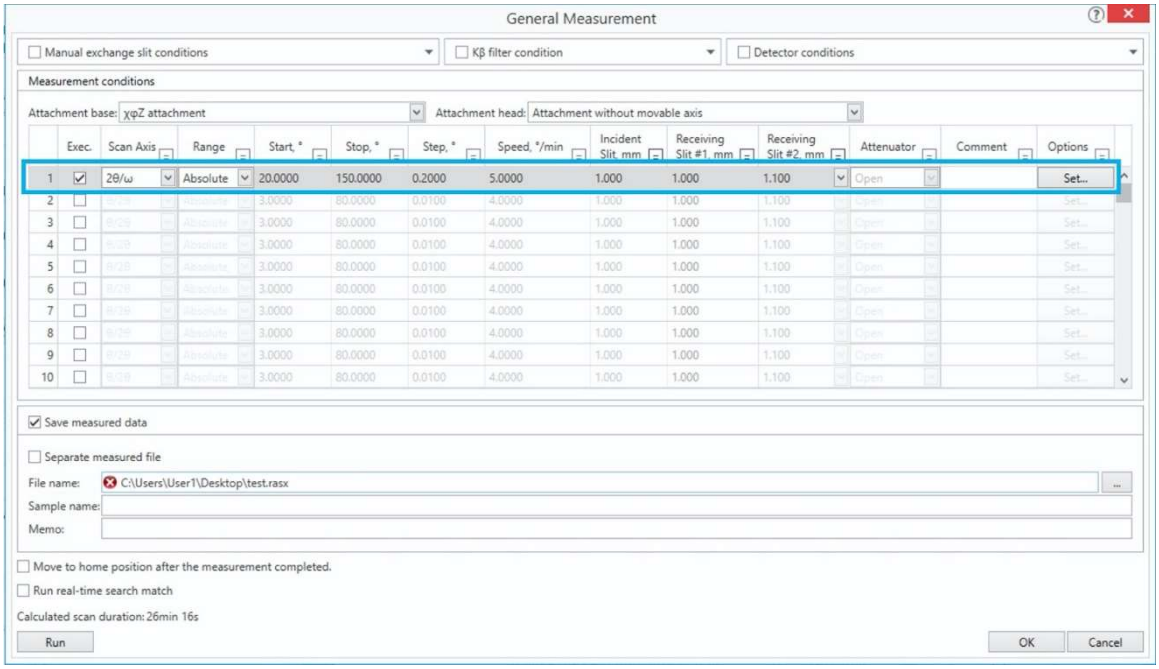

Reciprocal Space Map of the ZnO (205) reflex

j) Now we move to measure the reciprocal space map around the (205) reflex of ZnO. Because this is an asymmetric reflex, the angles of X-ray source θ_s and detector θ_d are not identical, but need to be offset by the τ angle. Look up the corresponding 2θ and τ values from Appendix B, and calculate $\theta_s = (2\theta/2) - \tau$ and $\theta_d = (2\theta/2) + \tau$. Record the calculated values and move them in the 'Pro Control' panel. Observe the relative positions of X-ray source and detector to the sample surface. Check if the 2θ-axis position in 'H/W Status' panel is correct.

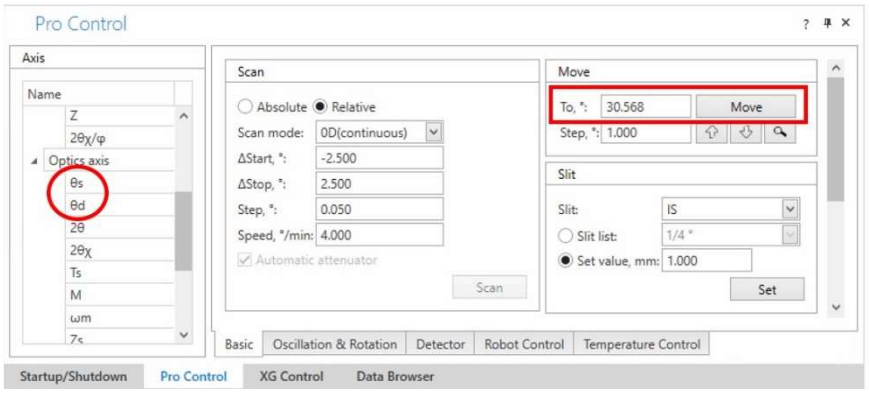

k) Perform a φ-scan with 0-360° absolute range, 1° step, and 180°/min speed. Record the optimized φ position after the scan.

l) Perform an ω-scan with a relative ±1° range, 0.02° step, and 1°/min speed. Record the new ω position.

m) Perform a $2\theta/\omega$ optimization scan with a relative ±0.5° range, 0.01° step, and 0.5°/min speed. Record the new $2\theta/\omega$ position.

n) From **Part Activities** panel, double-click **Measurement Activity / RSM Measurement** to add it to the **Sequence** panel. Open the settings of **RSM Measurement**, specify the file destination and select the 'Customized conditions' option.

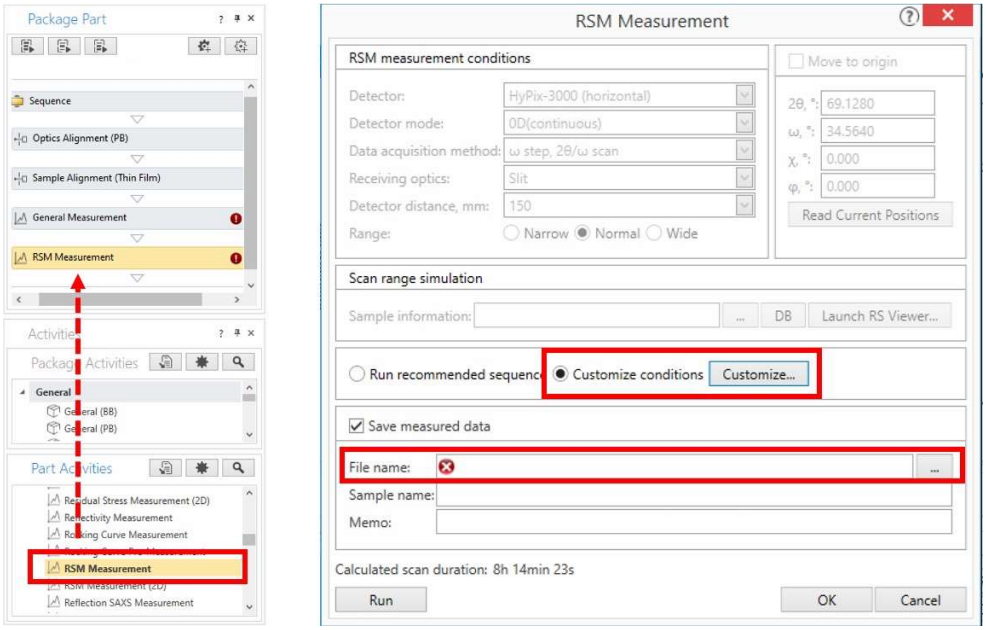

o) In the new settings window, select **'1D(single exposure)'** as the detector mode. Check the 'Move to origin' box and then 'Read Current Positions' – these values will vary based on your previous optimization steps. Change the slit setting to IS=1 mm, RS1=20 mm, and RS2=*Open*. Set the 2θ-axis range to be relative $\pm 2°$ – this will be covered by the length of the CCD detector and therefore no stepwise scan is required. Set the ω axis range to be relative $\pm 1°$ with 0.005° step and 1°/min speed. Execute the measurement and you can observe the slice images of RSM in real time.

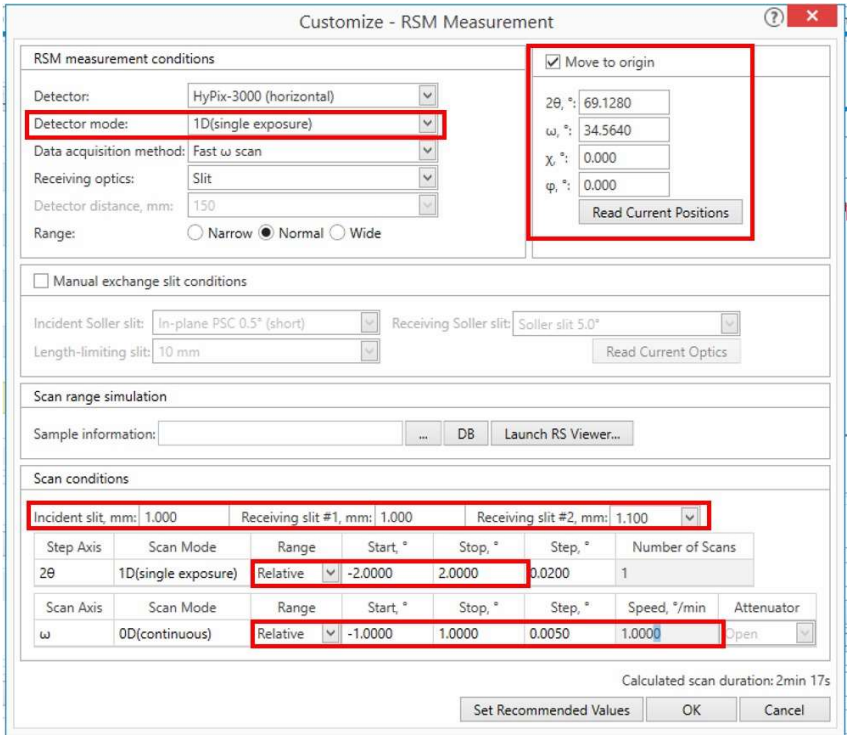

p) When the measurement is finished, select 'Chart / Axes:' and change the setting from 'Angular' to 'Reciprocal.' The just collected 2D data (ω, 2θ) will be converted to the reciprocal space ($Q_x/2\pi$, $Q_z/2\pi$).

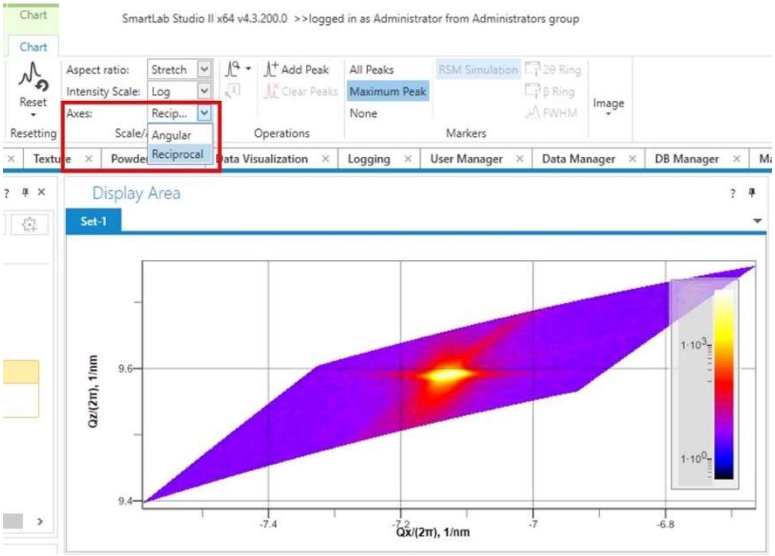

q) Right-click on the graph, select 'Export → Export Data' then specify the file destination. Pay attention to the unit difference from Equations (47) and (48).

6.5. Sample C

Determining the Mg content of $Zn_{1-x}Mg_xO$

a) Install Sample C onto the sample holder. Follow the same sample alignment procedure as described in section 6.2. Record the sample height *Z* value after the alignment.
b) Here, you will investigate the Mg content *x* for a $Zn_{1-x}Mg_xO$ sample. As the exact value of the *c*-lattice constant of Sample C is unknown, first you have to use the (006) reflex of sapphire (Al_2O_3) to correct the angular deviation from sample mounting. In 'Pro Control' panel, move the $\theta/2\theta$-axis to the 2θ value of the Al_2O_3 (006) reflex. Do a φ-scan with 0-360° absolute range, 1° step, and 180°/min speed. Record the optimized φ position after the scan. (Use the slit setting IS=1 mm, RS1=1 mm, and RS2=1.1 mm)
c) Perform an ω-scan with a relative $\pm$1° range, 0.004° step, and 1°/min speed. Record the new ω position.
d) Now, move the $2\theta/\omega$ axis to the expected 2θ value of the ZnO (006) reflex. Because Sample C is not pure ZnO and should have a quite different 2θ angle for its (006) reflex, you will need to find the actual peak by expanding the scan range. Perform a $2\theta/\omega$-scan with a relative $\pm$2.5° range, 0.05° step, and 2.5°/min speed. Record the new $2\theta/\omega$ position.
e) Perform an ω-scan with a relative $\pm$0.1° range, 0.002° step, and 0.1°/min speed. Record the new ω position.
f) Reduce the slit opening sizes to IS=0.05 mm, RS1=0.05 mm, and RS2=0.3 mm. Use the 'General Measurement' function to collect a $2\theta/\omega$-scan, with a relative range of $\pm$0.2°, 0.002° step, and 0.04°/min speed. Search for the peak position and export the file to .XY format.

6.6. Post-Measurement

Collect all the samples to the original container and clean the double side tapes from the wafer sample holder. Inform your instructor so that the X-ray diffractometer can be switched off. Use a USB dongle to bring the measurement results with you.

7. Report

1) Plot the long $2\theta/\omega$ scan of sample B in a logarithmic scale. Which peaks can you identify?
2) Estimate the layer thickness of sample A by using Equation (41).
3) Determine the layer thickness of sample B by using Equations (41) and (42). Compare the obtained values! Conclusion?
4) Estimate the screw-type dislocation densities of samples A and B and their lateral crystallite size. Compare the structural quality of both samples.
5) Estimate the edge-type dislocation density of sample A.
6) Illustrate graphically which lattice planes are associated with the (112) and the (113) reflexes respectively. Verify the epitaxial relation of ZnO on a *c*-plane sapphire substrate.
7) Determine the peak center of the ZnO (205) reflex. Determine the *a*- and *c*-lattice constants of sample B. Which mechanisms can you identify for the broadening of its (205) reflex? Calculate the lattice mismatch by assuming that the ZnO film on the sapphire substrate is fully relaxed and by taking into account the formation of a coincidence lattice.
8) Determine the *c*-lattice constant of sample C. Why was the 006-reflex instead of the (002) reflex used for this purpose? Sadofev et al. [4] demonstrated the validity of Vegard's rule and found for the variation of the *c*-lattice constant with the Mg-content *x* for $Zn_{1-x}Mg_xO$:

$$c_{Zn_{1-x}Mg_xO} = c_{ZnO} - x \cdot 0.17\text{Å} \tag{49}$$

Use this relation with the above determined value for c_{ZnO} to calculate the Mg-content of sample C. Estimate the error of the obtained result by assuming that the Equation (49) is accurate.

8. References

[1] K. Kopitzki. *Einführung in die Festkörperphysik.* Teubner Studienbücher, 3rd edition, 1993.

[2] B. E. Warren. *X-ray Diffraction*. Dover Publications, Inc., New York, 1st edition, 1990.

[3] C. G. Dunn and E. F. Koch. *Acta Metall.,* 5:584, 1957.

[4] S. Sadofev, S. Blumstengel, J. Cui, J. Puls, S. Rogaschewski, P. Schäfer, Y. G. Sadofyev, and F. Henneberger. Growth of high-quality ZnMgO epilayers and ZnO/ZnMgO quantum well structures by radical-source molecular-beam epitaxy on sapphire. *Applied Physics Letters*, 87:091903, 2005.

[5] H. Vogel. *Gerthsen Physik*. Springer-Verlag, 20th edition, 1999.

Appendix A Measurement Report Sheet

Measurement Record – Sample A *Sample height $Z =$*

Scan Axis	Range [°]	Step [°]	Speed [°/min]	Slit [mm]			Result
				IS	RS1	RS2	
ZnO (002)							$\theta/2\theta =$
φ	0-360	1	180	1	1	1.1	$\varphi =$
ω	±1	0.02	1	1	1	1.1	$\omega =$
$2\theta/\omega$	±0.5	0.01	0.5	0.05	0.05	0.3	$2\theta/\omega =$
ω	±0.5	0.01	0.5	0.05	0.05	0.3	$\omega =$
$2\theta/\omega$	±0.2	0.004	0.2	0.05	0.05	0.3	$2\theta/\omega =$
ZnO (101)	skewed geometry			$\chi =$			$\theta/2\theta =$
φ	0-360	1	180	1	1	1.1	$\varphi =$
φ	±2	0.04	2	1	1	1.1	$\varphi =$
χ	±2	0.04	2	1	1	1.1	$\chi =$
ω	±2	0.04	2	1	1	1.1	$\omega =$
$2\theta/\omega$	±1.5	0.03	1.5	0.2	0.2	0.3	$2\theta/\omega =$
ω	±1.5	0.03	1.5	0.2	0.2	0.3	$\omega =$
ZnO (112)	skewed geometry			$\chi =$			$\theta/2\theta =$
φ	0-360	1	180	1	1	1.1	
Al_2O_3 (113)	skewed geometry			$\chi =$			$\theta/2\theta =$
φ	0-360	0.5	90	1	1	1.1	

Measurement Record – Sample B *Sample height $Z =$*

Scan Axis	Range [°]	Step [°]	Speed [°/min]	Slit [mm]			Result
				IS	RS1	RS2	
ZnO (002)							$\theta/2\theta =$
φ	0-360	1	180	1	1	1.1	$\varphi =$
ω	±0.5	0.005	0.5	1	1	1.1	$\omega =$
$2\theta/\omega$	±0.5	0.005	0.5	1	1	1.1	$2\theta/\omega =$
ω	±0.2	0.002	0.2	0.05	0.05	0.3	$\omega =$
$2\theta/\omega$	±0.3	0.002	0.3	0.05	0.05	0.3	$2\theta/\omega =$
ω	±0.05	0.0002	0.05	0.05	0.05	0.3	$\omega =$
$2\theta/\omega$	±0.5	0.001	0.2	0.05	0.05	0.3	$2\theta/\omega =$
$2\theta/\omega$	20-150	0.2	5	1	1	1.1	Wide range measurement
ZnO (205)	asymmetric geometry			$\theta_s =$	$\theta_d =$		$\omega =$ $2\theta =$
φ	0-360	1	180	1	1	1.1	$\varphi =$
ω	±1	0.02	1	1	1	1.1	$\omega =$
$2\theta/\omega$	±0.5	0.01	0.5	1	1	1.1	$2\theta/\omega =$
2θ	±2	Single exposure		1	20	Open	Reciprocal space mapping (1D detection, single exposure)
ω	±1	0.002	0.2				

Measurement Record – Sample C *Sample height* $Z =$

Scan Axis	Range [°]	Step [°]	Speed [°/min]	Slit [mm]			Result
				IS	RS1	RS2	
Al_2O_3 (006)							$\theta/2\theta =$
φ	0-360	1	180	1	1	1.1	$\varphi =$
ω	$\pm$1	0.004	1	1	1	1.1	$\omega =$
ZnO (006)							$2\theta/\omega =$
$2\theta/\omega$	$\pm$2.5	0.05	2.5	1	1	1.1	$2\theta/\omega =$
ω	$\pm$0.1	0.002	0.1	1	1	1.1	$\omega =$
$2\theta/\omega$	$\pm$0.2	0.002	0.04	0.05	0.05	0.3	$2\theta/\omega =$

Appendix B Theoretical 2θ and τ values of ZnO and Al_2O_3

ZnO				a = 3.2475 Å c = 5.2024 Å λ = 1.540598 Å
h	k	l	2θ [°]	Offset τ [°]
0	0	1	17.0298	0.0000
0	0	2	34.4510	0.0000
0	0	3	52.7443	0.0000
0	0	4	72.6360	0.0000
0	0	5	95.5195	0.0000
0	0	6	125.3454	0.0000
1	0	1	36.2817	61.6046
1	0	2	47.5788	42.7658
1	0	3	62.9133	31.6581
1	0	4	81.4654	24.8182
1	0	5	104.2539	20.3025
1	0	6	136.7639	17.1346
2	0	1	69.1444	74.8747
2	0	2	77.0282	61.6046
2	0	3	89.7001	50.9616
2	0	4	107.5595	42.7658
2	0	5	134.1325	36.4986
3	0	1	113.2135	79.7852
3	0	2	121.7154	70.1811
3	0	3	138.1535	61.6046
1	1	1	59.5991	72.6663
1	1	2	68.0062	58.0265
1	1	3	81.0676	46.8830
1	1	4	98.7233	38.6944
1	1	5	123.1126	32.6514

*Based on Equations (22) and (28)

Al_2O_3				a = 4.7577 Å c = 12.9907 Å λ = 1.540598 Å
h	k	l	2θ [°]	Offset τ [°]
0	0	3	20.4937	0.0000
0	0	6	41.6823	0.0000
0	0	9	64.5072	0.0000
0	0	12	90.7234	0.0000
0	0	15	125.6071	0.0000
1	0	2	25.5820	57.6115
1	0	4	35.1564	38.2459
1	0	5	41.0363	32.2345
1	0	8	61.3119	21.5099
1	0	11	85.4568	15.9936
1	0	14	116.6280	12.6916
2	0	10	89.0158	32.2345
2	0	13	117.9070	25.8761
3	0	12	129.9224	38.2459
4	0	8	124.6458	57.6115
4	0	11	165.7720	48.9045
1	1	0	37.7873	90.0000
1	1	3	43.3644	61.2177
1	1	6	57.5112	42.3071
1	1	9	77.2505	31.2482
1	1	12	102.8461	24.4693
1	1	15	142.3663	20.0047
2	2	0	80.7256	90.0000
2	2	3	84.3832	74.6411
2	2	6	95.2782	61.2177
2	2	9	114.1066	50.5104
2	2	12	148.3703	42.3071